Research Square

Preprints are preliminary reports that have not undergone peer review.
They should not be considered conclusive, used to inform clinical practice,
or referenced by the media as validated information.

Nobiletin-Loaded Chitosan Nanoparticles Attenuate Doxorubicin-Induced Cardiotoxicity Through Modulation of Nrf2/HO-1, NF-κB, Mitochondrial Dysfunction, Apoptosis, and Ferroptosis

Ekramy M. Elmorsy
Northern Border University
Amina A Farag
Benha University
Maha M. Mokhtar
Benha University
Enas Elgendy
Benha University
Hend R. Mousa
Benha University
Taghrid G. Kharboush
Benha University
Ola A. Habotta
Mansoura University
Petra Rocic
pxr037@shsu.edu
Sam Houston State University

Research Article

Keywords: Nobiletin, Chitosan nanoparticles, Doxorubicin cardiotoxicity, Oxidative stress, Ferroptosis, Cardioprotection

Posted Date: November 24th, 2026

DOI: https://doi.org/10.21203/rs.3.rs-11197013/v1

License: This work is licensed under a Creative Commons Attribution 4.0 International License.
Read Full License

Additional Declarations: No competing interests reported.

Nobiletin-Loaded Chitosan Nanoparticles Attenuate Doxorubicin-Induced Cardiotoxicity Through Modulation of Nrf2/HO-1, NF-κB, Mitochondrial Dysfunction, Apoptosis, and Ferroptosis

Ekramy M. Elmorsy[1], Amina A Farag[2], Maha M. Mokhtar[3,4], Enas Elgendy[5], Hend R. Mousa[6], Taghrid G. Kharboush[7], Ola A.Habotta[8,9], Petra Rocic[10]

[1]Center for Health Research, Northern Border University, P.O. Box 1321, Arar 91431, Saudi Arabia; Ekramy.elmorsy@nbu.edu.sa
[2]Department of Forensic Medicine and Clinical Toxicology, Faculty of Medicine, Benha University, Benha, Egypt, Amina.farag@fmed.bu.edu.eg
[3]Department of Forensic Medicine and Clinical Toxicology, Faculty of Medicine, Benha University, Benha 13518, Egypt; Maha.mahmoud@fmed.bu.edu.eg
[4]Department of Forensic Medicine and Clinical Toxicology, Faculty of Medicine, Delta University for Science and Technology, Gamasa 11152, Egypt.
[5]Department of Histology, Faculty of Medicine, Benha University, Benha 13518, Egypt; enas.elgendy@fmed.bu.edu.eg
[6]Anatomy & Embryology Department, faculty of medicine, Benha University, Benha 13518, Egypt; drhendragab@yahoo.com
[7]Department of Medical Microbiology and Immunology, Faculty of Medicine, Benha University, Benha, 13518, Egypt; taghreed.abdelrahman@fmed.bu.edu.eg
[8]Department of Forensic Medicine and Toxicology, Faculty of Veterinary Medicine, Mansoura University, Mansoura 35516, Egypt; email: ola_ali@mans.edu.eg
[9]Horus Research Center, Horus University—Egypt (HUE), New Damietta 34518, Egypt
[10]Department of Physiology and Pharmacology, Sam Houston State University, Russel and Glenda Gordy College of Osteopathic Medicine, Conroe, TX 77304, USA; pxr037@shsu.edu

Corresponding author: Petra Rocic, PhD
Department of Physiology and Pharmacology
Sam Houston State University
Russell and Glenda Gordy College of Osteopathic Medicine
925 City Central Avenue
Conroe, TX 77304
Email: pxr037@shsu.edu
Phone: 936-202-5299

Abstract:

Doxorubicin (DOX)-induced cardiotoxicity involves interconnected oxidative, inflammatory, mitochondrial, apoptotic, and ferroptosis-related mechanisms. Nobiletin (NOB), a citrus-derived polymethoxyflavone, exhibits antioxidant and anti-inflammatory properties, but its therapeutic application may be constrained by unfavorable physicochemical and pharmacokinetic properties. This study investigated whether chitosan nanoencapsulation enhances NOB-mediated cardioprotection and explored the involvement of Nrf2, NF-κB, mitochondrial, and ferroptosis-related pathways. Eighty male Wistar rats were allocated to eight groups: control, chitosan, NOB, NOB-loaded chitosan nanoparticles (NOB-CHNPs), DOX, DOX + chitosan, DOX + NOB, and DOX + NOB-CHNPs. NOB and NOB-CHNPs were administered orally at 20 mg/kg/day for four weeks, while DOX was administered intraperitoneally at a cumulative dose of 15 mg/kg during the final two weeks. DOX induced cardiac injury accompanied by oxidative stress, NF-κB-associated inflammation, mitochondrial dysfunction, apoptosis, and ferroptosis-related alterations, including dysregulation of Nrf2/HO-1, SIRT1/PGC-1α, and ACSL4/GPX4/SLC7A11 signaling. NOB attenuated these alterations, while NOB-CHNPs generally produced greater effects and better preserved myocardial histology and mitochondrial ultrastructure. Complementary cardiomyocyte experiments using ML385, BAY 11-7082, ferrostatin-1 (Fer-1), and RSL3 provided pharmacological evidence supporting the involvement of Nrf2, NF-κB, and ferroptosis-related mechanisms. ML385 attenuated NOB-CHNP-mediated protection, whereas Fer-1 reproduced key protective responses. NOB-CHNPs reduced DOX-induced C11-BODIPY oxidation from 48.0% to 9.83% ($p < 0.0001$), while RSL3 partially reversed this effect (36.0%; $p < 0.0001$ vs. NOB-CHNPs). Collectively, NOB-CHNPs provided greater cardioprotection than free NOB against DOX-induced cardiac injury, with pharmacological intervention supporting contributions from Nrf2-dependent antioxidant defense, NF-κB-associated inflammation, mitochondrial homeostasis, and GPX4-related ferroptosis regulation**.**

Keywords: Nobiletin; Chitosan nanoparticles; Doxorubicin cardiotoxicity; Oxidative stress; Ferroptosis; Cardioprotection

Introduction:

Doxorubicin (DOX) is a widely used chemotherapeutic agent with broad anticancer activity (Aryal and Rao 2016). Despite its therapeutic benefits, its clinical use is limited by its potential to cause cardiotoxicity. Cardiac injury may occur during treatment or after completion of therapy (Belger et al. 2024; Bhutani et al. 2025). In severe cases, DOX-induced cardiac damage can progress to systolic dysfunction and heart failure (Bhutani et al. 2025). Therefore, preventing or reducing DOX-related cardiac injury remains an important therapeutic challenge. Several mechanisms are involved in DOX-induced cardiotoxicity. Among them, oxidative stress is considered a major contributor to cardiac injury (Wang et al. 2021). DOX can increase the generation of reactive oxygen species (ROS) and, at the same time, impair the endogenous antioxidant defense system (Kong et al. 2022). This imbalance can increase oxidative damage in cardiac tissue and contribute to the progression of DOX-induced myocardial injury. The heart is especially susceptible to oxidative stress. Cardiomyocytes have high energy requirements and depend largely on mitochondrial oxidative metabolism to sustain continuous contraction (Ulmer et al. 2018).

Mitochondria are essential for meeting the high energy demands of cardiac tissue. Their integrity is therefore critical for normal cardiomyocyte function (Ulmer et al. 2018). DOX can disrupt mitochondrial homeostasis, impair energy metabolism, and increase the vulnerability of cardiomyocytes to cellular stress (Sharma et al. 2026). Mitochondrial dysfunction can interact with other pathological processes, especially oxidative stress and inflammation (Vitale et al. 2024). It can also contribute to dysregulated cell death, which may further promote cardiac injury (Wang et al. 2021). Together, these interconnected processes can contribute to the progressive decline in cardiac function. Thus, mitochondrial injury is an important component of the multifactorial mechanisms underlying DOX-induced cardiotoxicity.

Growing evidence suggests that ferroptosis may contribute to cardiovascular injury and represents an additional form of regulated cell death alongside apoptosis (Huang et al. 2023a; Li et al. 2024). Ferroptosis differs from other forms of cell death because it depends on iron-driven lipid peroxidation (Aguilera et al. 2022). This process can damage cellular membranes and impair cardiomyocyte function (Huang et al. 2023a). These features make ferroptosis a potentially important mechanism in cardiovascular injury. Maintaining lipid redox balance is essential for protecting cells from ferroptotic damage. GPX4 is an important defense mechanism because it

limits the accumulation of lipid hydroperoxides (Yoo et al. 2010). When these protective systems are impaired, cardiomyocytes may become more vulnerable to toxic stress. This disruption may contribute to the complex mechanisms involved in DOX-induced cardiotoxicity (Li et al. 2024).

Natural bioactive compounds have gained considerable attention as potential cardioprotective agents because of their antioxidant and anti-inflammatory activities (Tomou et al. 2023). Nobiletin (NOB) is a polymethoxylated flavone abundant in citrus peels (Matsuzaki and Ohizumi 2021)with reported antioxidant, anti-inflammatory, anti-apoptotic, and metabolic regulatory properties (Çetinkaya et al. 2026; Huang et al. 2023b; Murata et al. 2023). Previous evidence has indicated a protective effect of free NOB against DOX-induced cardiac injury; however, this work focused primarily on apoptosis-related cardioprotection. Consequently, whether NOB influences the broader interconnected processes underlying DOX cardiotoxicity, particularly oxidative stress, inflammatory signaling, mitochondrial dysfunction, and ferroptosis, remains insufficiently characterized.

The potential application of NOB is also challenged by its poor water solubility and low bioavailability (Ju et al. 2022). Nanotechnology-based formulations represent a potential approach for improving the physicochemical and biological performance of poorly soluble bioactive compounds (Kuskov et al. 2025). Chitosan nanoparticles are particularly attractive because of their biocompatibility, biodegradability, and suitability for encapsulating poorly water-soluble compounds (Bashir et al. 2022; El-Saadony et al. 2025). Nevertheless, the cardioprotective efficacy of NOB-loaded chitosan nanoparticles (NOB-CHNPs) against DOX-induced cardiotoxicity and their comparative effects relative to free NOB have not been adequately investigated. Moreover, the potential contribution of ferroptosis-related signaling to NOB-mediated protection against DOX cardiotoxicity remains poorly defined.

Accordingly, the novelty of the present study lies in the direct comparison of free NOB with NOB-CHNPs and the integrated evaluation of oxidative stress, NF-κB-associated inflammation, mitochondrial dysfunction, apoptosis, and ferroptosis-related alterations in DOX-induced cardiac injury. To extend the in vivo findings and strengthen mechanistic interpretation, complementary cardiomyocyte experiments using the Nrf2 inhibitor ML385, NF-κB inhibitor BAY 11-7082, ferroptosis inhibitor ferrostatin-1, and GPX4 inhibitor RSL3 were conducted to pharmacologically interrogate the involvement of Nrf2, NF-κB, and ferroptosis-related pathways. Therefore, the present study aimed to determine whether chitosan nanoencapsulation enhances the

cardioprotective effects of NOB against DOX-induced cardiotoxicity and to investigate the contribution of Nrf2/HO-1 and NF-κB signaling, mitochondrial homeostasis, apoptosis, and ACSL4/GPX4/SLC7A11-associated ferroptotic processes to this protection.

Material and methods:

Preparation of Nobiletin-Loaded Chitosan Nanoparticles

Nobiletin-loaded chitosan nanoparticles (NOB-CHNPs) were prepared using the ionic gelation method with sodium tripolyphosphate (TPP) as the cross-linking agent, following a previously described procedure with minor modifications (Rahaeng et al. 2026). Briefly, 100 mg of chitosan was dissolved in 10 mL of 1% acetic acid and stirred until a homogeneous solution was obtained. Tween 80 was then added at a final concentration of 1%, followed by sonication for 15 min. The pH was adjusted to 5.0 using 2 N NaOH. Nobiletin (30 mg) was added to the chitosan dispersion under continuous stirring. The mixture was then briefly sonicated to facilitate uniform dispersion of NOB while minimizing heat generation. Separately, 20 mg of sodium TPP was dissolved in deionized water and added dropwise to the NOB-containing chitosan solution under continuous magnetic stirring. The mixture was further stirred for 60 min to allow nanoparticle formation through ionic cross-linking. The formed NOB-CHNPs were collected by centrifugation at 15,000 rpm for 30 min, washed with deionized water to remove unencapsulated NOB and residual formulation components, and freeze-dried and stored until subsequent characterization and experimental use.

Characterization of Nobiletin-Loaded Chitosan Nanoparticles

The prepared NOB-CHNPs were characterized for hydrodynamic particle size, polydispersity index (PDI), and zeta potential using a Zetasizer Nano ZS. Samples were appropriately diluted with distilled water before measurement, and measurements were performed in triplicate. Particle size was reported as the Z-average hydrodynamic diameter. The morphology and structural features of the nanoparticles were examined by transmission electron microscopy (TEM; JEOL JEM-2100, Japan) operated at 160 kV.

Encapsulation Efficiency and Drug Loading

The encapsulation efficiency (EE%) and drug loading (DL%) of NOB-CHNPs were determined by quantifying the amount of NOB associated with the recovered nanoparticles. EE% was calculated as the amount of encapsulated NOB relative to the initial amount of NOB used in

the formulation, whereas DL% was calculated as the amount of encapsulated NOB relative to the total weight of the recovered nanoparticles. The following equations were applied:

EE (%) = (amount of encapsulated NOB / initial amount of NOB) × 100

DL (%) = (amount of encapsulated NOB / total weight of recovered NOB-CHNPs) × 100

The experimentally determined NOB content was subsequently used to calculate the amount of NOB-CHNPs required to provide an NOB-equivalent dose of 20 mg/kg.

In Vitro NOB Release

The in vitro release profile of NOB from NOB-CHNPs was evaluated using a dialysis membrane method. A known amount of NOB-CHNPs equivalent to 20 mg of NOB was dispersed in the release medium and transferred into a dialysis membrane, which was sealed and immersed in the release medium at 37 °C under continuous agitation.

Samples of the external medium were collected at predetermined time intervals, and an equal volume of fresh release medium was added after each withdrawal to maintain the experimental volume. Released NOB was quantified using the selected analytical method. Cumulative drug release was calculated after accounting for sequential sample withdrawal and expressed as the percentage of the total NOB incorporated into the nanoparticles.

Fourier Transform Infrared Spectroscopy (FTIR)

FTIR analysis was performed to evaluate the chemical characteristics and potential interactions among NOB, chitosan, and the formulated NOB-CHNPs. Samples were analyzed using an FTIR spectrometer (PerkinElmer, Waltham, MA, USA), and spectra were recorded over the range of 4000–400 cm^{-1}. The characteristic absorption bands of free NOB and chitosan were compared with those observed in the NOB-CHNP formulation, with particular attention to band shifts, changes in intensity, or broadening that could indicate interactions associated with nanoparticle formation.

Storage Stability of NOB-CHNPs

The physical stability of NOB-CHNPs was evaluated during storage at 4 °C for 30 days. Particle size, PDI, and zeta potential were determined on days 0, 7, 14, 21, and 30. Changes in these physicochemical parameters relative to baseline were used to assess the physical stability of the formulation throughout the storage period.

Animal Husbandry

Eighty healthy adult male Wistar albino rats, weighing 200–250 g at the beginning of the study, were obtained from the Medical Experimental Research Center (MERC), Faculty of Medicine, Mansoura University. Male rats were selected to minimize variability associated with sex-dependent hormonal fluctuations and to provide a more homogeneous experimental population for evaluating DOX-induced cardiotoxicity and treatment-related responses. The exclusive use of males should therefore be considered when extrapolating the findings across sexes. Before experimental procedures commenced, the animals were acclimatized to the laboratory environment for one week. Rats were housed in stainless-steel cages under controlled conditions at 25 ± 2 °C with a 12-h light/12-h dark cycle. Standard rodent chow supplied by El-Nasr Pharmaceuticals and Chemicals Industry, Egypt, and drinking water were provided ad libitum throughout the study.

Experimental Design

The animals were randomly assigned to eight experimental groups, with 10 animals per group. Group allocation was performed using a computer-generated random-number sequence to minimize selection bias. The required sample size was estimated a priori using G*Power version 3.1.9.7 for a one-way ANOVA with eight groups, assuming a large effect size (f = 0.40), a two-sided α level of 0.05, and 80% statistical power. The analysis indicated a minimum total sample size of approximately 97 animals. However, the present experiment included 80 animals (10 per group), based on the predefined experimental design and feasibility considerations. The experiment continued for 4 weeks. The DOX-induced cardiac injury model was established according to the protocol described by (Arafa et al. 2014), whereas the NOB dose was selected based on the study of Sunagawa et al. (2025). DOX was administered intraperitoneally at 2.5 mg/kg per injection for six injections during the final 2 weeks, yielding a cumulative dose of 15 mg/kg. This regimen was selected because repeated intraperitoneal administration provides a reproducible experimental model of cumulative DOX-induced cardiotoxicity while avoiding the acute toxicity associated with a single high dose. NOB was administered orally at 20 mg/kg/day to reflect the enteral route commonly used for this bioactive compound and to permit direct comparison between free NOB and the NOB-CHNP formulation at an equivalent NOB dose. The same NOB-equivalent dose was maintained for the nanoparticle formulation to ensure that any differences between free and nanoencapsulated NOB were related to formulation rather than dose. NOB-based treatments were initiated 2 weeks before DOX exposure and continued during DOX

administration to assess their preventive and concomitant protective effects against developing cardiac injury.

- Group 1 (Control): Rats received 0.9% normal saline by intraperitoneal injection for 2 weeks.
- Group 2 (Chitosan): Rats received chitosan alone for 4 weeks using the same administration schedule and vehicle applied to the nanoparticle formulation.
- Group 3 (NOB): Rats received free NOB at 20 mg/kg body weight/day by oral gavage for 4 weeks. NOB was suspended in distilled water immediately before administration.
- Group 4 (NOB-CSNPs): Rats received NOB-loaded chitosan nanoparticles orally for 4 weeks at a dose equivalent to 20 mg/kg body weight/day of NOB.
- Group 5 (DOX): Rats received DOX at 2.5 mg/kg body weight by intraperitoneal injection. Six injections were administered over the final 2 weeks, resulting in a cumulative dose of 15 mg/kg body weight. DOX was dissolved in 0.9% normal saline before administration.
- Group 6 (DOX + Chitosan): Rats received chitosan alone for 4 weeks, with DOX administration during the final 2 weeks. DOX was given intraperitoneally at 2.5 mg/kg body weight per injection for a total of six injections.
- Group 7 (DOX + NOB): Rats received NOB at 20 mg/kg body weight/day by oral gavage for 4 weeks. NOB was administered in distilled water, beginning 2 weeks before DOX exposure and continuing throughout the 2-week DOX treatment period. DOX was administered intraperitoneally at 2.5 mg/kg body weight per injection for six injections.
- Group 8 (DOX + NOB-CSNPs): Rats received NOB-loaded chitosan nanoparticles for 4 weeks at a dose equivalent to 20 mg/kg body weight/day of NOB. Treatment started 2 weeks before DOX administration and continued during the subsequent 2 weeks of DOX exposure. DOX was administered at 2.5 mg/kg body weight by intraperitoneal injection for six injections.

For Groups 3, 4, 7, and 8, the test formulations were administered for the full 4-week period. In the DOX-treated groups, DOX exposure was restricted to the final 2 weeks. Thus, the NOB-based treatments provided a 2-week pretreatment period before DOX exposure and continued concomitantly with DOX administration.

Sample Collection and Tissue Preparation

Biological samples were collected 24 h after administration of the final treatment. Rats were fasted overnight with free access to water before sampling. Anesthesia was induced with isoflurane delivered in oxygen using an induction chamber and was maintained at an appropriate concentration during blood collection. Adequate depth of anesthesia was confirmed by loss of the righting reflex and absence of withdrawal responses to a firm paw or toe pinch. Blood was collected from the retro-orbital venous plexus into plain tubes for serum preparation and sodium citrate tubes for plasma collection. While the animals remained deeply anesthetized, euthanasia was performed by increasing isoflurane to 5% in oxygen and maintaining exposure until complete cessation of spontaneous respiration. Death was subsequently confirmed by the absence of respiratory movements and cardiac activity before tissue harvesting. For serum preparation, blood samples were centrifuged at 850 × *g* for 15 min immediately after collection. The resulting serum was aliquoted into labeled Eppendorf tubes and stored at −20 °C until biochemical analysis. Hearts were excised, rinsed in ice-cold normal saline and processed according to the planned analyses. Left ventricular tissue was homogenized in ice-cold phosphate-buffered saline (0.1 M, pH 7.4) at a tissue-to-buffer ratio of 1:10 (w/v). Tissue homogenates were centrifuged at 850 × *g* for 15 min, supernatants collected and stored at −20 °C until analysis.

For morphological assessment, hearts from six rats per group were fixed in 20% neutral buffered formalin for histopathological and immunohistochemical examination, whereas cardiac specimens from four rats per group were fixed immediately in 2.5% glutaraldehyde for transmission electron microscopy (TEM). Thus, the biological sample size was n = 6 rats/group for histopathological assessment and n = 4 rats/group for ultrastructural examination, with individual animals considered the biological replicates.

Serum Cardiac Injury Biomarkers

Cardiac troponin T (cTnT) was quantified using a rat-specific ELISA kit by Kamiya Biomedical (Seattle, WA, USA). The assay was conducted according to the procedure reported by Katus et al. (1991). CK-MB was analyzed separately using a colorimetric diagnostic kit obtained from Spinreact (Sant Esteve de Bas, Girona, Spain). Myoglobin was quantified with a rat-specific ELISA kit from Assay Genie (Dublin, Ireland; Cat. No. RTFI00975). LDH was measured using a rat-specific ELISA kit from Assay Genie (Cat. No. AEKE09291). Each assay was carried out following the relevant manufacturer's protocol. For the ELISA-based measurements, serum values were obtained from the standard curves supplied with the respective kits.

Assessment of Myocardial Oxidative Stress

Oxidative stress and antioxidant status were assessed in cardiac tissue homogenates. Commercial colorimetric assay kits were used to measure reduced glutathione (GSH), superoxide dismutase (SOD), catalase (CAT), and malondialdehyde (MDA). The GSH assay kit (GR 2511), SOD kit (SOD 2521), CAT kit (CA 2517), and MDA kit (MD 2529) were obtained from BioDiagnostic (Giza, Egypt). All assays were performed according to the manufacturer's instructions. Oxidative DNA damage was evaluated by measuring 8-hydroxy-2′-deoxyguanosine (8-OHdG). A rat-specific ELISA kit was obtained from MyBioSource (San Diego, CA, USA; Cat. No. MBS269902). The antioxidant response was further assessed by measuring nuclear factor erythroid 2-related factor 2 (Nrf2) and heme oxygenase-1 (HO-1). Both markers were determined using rat-specific ELISA kits from MyBioSource (Cat. Nos. MBS3807961 and MBS2024438, respectively). All measurements were conducted following the manufacturers' protocols.

Assessment of Myocardial Inflammation

Myocardial inflammation was assessed by measuring selected pro-inflammatory cytokines and the key inflammatory regulator nuclear factor-kappa B (NF-κB). Tumor necrosis factor-alpha (TNF-α), interleukin-6 (IL-6), and interleukin-1 beta (IL-1β) were quantified using rat-specific ELISA kits from Assay Genie. The corresponding kit catalog numbers were AEES00516 for TNF-α, RTES00015 for IL-6, and AEES02613 for IL-1β. NF-κB levels were determined using a rat ELISA kit from MyBioSource (Cat. No. MBS453975). All assays were performed according to the manufacturers' instructions. The concentrations of the measured inflammatory markers were calculated from the standard curves provided with the respective kits. The obtained values were normalized to the total protein content.

Assessment of Mitochondrial Dysfunction

Mitochondrial status in cardiac tissue was evaluated by measuring SIRT1, PGC-1α, cytochrome c, and ATP. These parameters were selected to provide complementary information on mitochondrial regulation, energy metabolism, and mitochondrial integrity.

Cardiac SIRT1 levels were determined using a rat-specific ELISA kit obtained from Assay Genie (Cat. No. RTF101128). PGC-1α concentrations were measured using a rat-specific ELISA kit from FineTest (Cat. No ER0455). Cytochrome c levels were quantified using a rat-specific ELISA kit supplied by Assay Genie (Cat. No. RTF100721). Cardiac ATP-citrate lyase (ACLY) protein levels were determined using a rat-specific ACLY ELISA kit (FineTest, Cat. No. ER0529).

All ELISAs were performed in homogenized cardiac tissue samples according to protocols provided by the respective manufacturers. Concentrations were calculated from the standard curves supplied with the kits and normalized to the total protein content.

Evaluation of Cardiac Apoptosis-Related Markers

The apoptotic status of the myocardium was determined by assessing changes in Bax, Bcl-2, and caspase-3. Cardiac tissue concentrations were measured using rat-specific ELISA kits purchased from MyBioSource. The Bax, caspase-3, and Bcl-2 kits were assigned Cat. Nos. MBS2512405, MBS729893, and MBS2515143, respectively. Following tissue analysis, the measured values were adjusted according to the total protein content of each cardiac sample. Concentrations were determined by reference to the standard curves supplied with the individual kits. All procedures were performed in accordance with the manufacturer's instructions.

Assessment of Ferroptosis-Related Markers

The involvement of ferroptosis in cardiac injury was investigated using a panel of biochemical markers. These included lipid peroxide (LPO), 4-hydroxynonenal (4-HNE), ferrous iron (Fe^{2+}), glutathione peroxidase 4 (GPX4), solute carrier family 7 member 11 (SLC7A11), and acyl-CoA synthetase long-chain family member 4 (ACSL4). Together, these markers provide complementary information on iron accumulation, lipid peroxidation, and the cellular defense mechanisms associated with ferroptotic injury. Cardiac LPO was quantified using a rat-specific ELISA kit (Assay Genie, Dublin, Ireland; Cat. No. AEKE11537). Cardiac 4-HNE levels were measured using a rat-specific ELISA kit (MyBioSource; Cat. No. MBS7606779). The cardiac Fe^{2+} content was determined using a colorimetric iron assay kit (Abcam, UK; Cat. No. ab83366). GPX4 was analyzed using a rat-specific ELISA kit from Biomatik (Cat. No. EKU12535), with the findings further confirmed using a RedDot Biotech ELISA kit (Cat. No. RD-GPX4-Ra). SLC7A11 and ACSL4 were measured using rat-specific ELISA kits from MyBioSource (Cat. Nos. MBS7204860 and MBS8820647, respectively). For all tissue-based assays, the analyses were conducted following the manufacturers' protocols. ELISA measurements were calculated from the corresponding standard curves and normalized to the total protein concentrations.

Quantitative Real-Time PCR Analysis

The transcriptional response of genes associated with antioxidant defense, inflammation, and ferroptosis was evaluated by quantitative real-time PCR (qRT-PCR). Cardiac tissue samples were processed for RNA extraction. Total RNA was isolated using QIAzol Lysis Reagent (Qiagen,

Hilden, Germany). Tissue disruption and homogenization were performed with a TissueLyser II. Chloroform was subsequently added to the homogenates to separate the RNA-containing aqueous phase. RNA was recovered by isopropanol precipitation and dissolved in nuclease-free water. RNA concentration and purity were assessed spectrophotometrically. Equal RNA inputs were used for subsequent reverse transcription.

Complementary DNA (cDNA) was synthesized using the iScript™ cDNA Synthesis Kit (Bio-Rad, Hercules, CA, USA). The resulting cDNA served as the template for qRT-PCR. Amplification was performed using iTaq Universal SYBR® Green Supermix (Bio-Rad; Cat. No. 172-5121) on a Rotor-Gene Q Real-Time PCR System (Qiagen, Germany). The thermal protocol included an initial denaturation step at 95 °C for 3 min, followed by 40 amplification cycles. Each cycle consisted of denaturation at 95 °C for 15 s, annealing at 58–60 °C for 30 s, and extension at 72 °C for 30 s. Product specificity was verified by melting-curve analysis over a temperature range of 65–95 °C.

β-actin was used as the reference gene for normalization. Relative gene expression was determined using the comparative Ct method and calculated according to the $2^{-\Delta\Delta Ct}$ formula (Livak and Schmittgen 2001). Three replicates were analyzed for each sample. The primer sequences for all target genes are shown in **Table 1.**

Table 1. Target genes and corresponding oligonucleotide primer sequences used for quantitative assessment of studied molecular pathways by real-time PCR.

Gene	Sequences (5′-3′)	Accession no	Length (bp)
Nrf2	F:TTTGTAGATGACCATGAGTCGC R: TCCTGCCAAACTTGCTCCAT	NM_031789.2	161
NF-κB	F: AGTCCCGCCCCTTCTAAAAC R: CAATGGCCTCTGTGTAGCCC	NM_001276711.1	106
GPX4	F: ATTCGCAGCCAAGGACATCG R: TGCAAGGGAAGGCCAGGATT	NM_017165.2	121
SLC7A11	F: AACTGCTGGTAATACGCCCC R: GGAAAATCTGGATCCGGGCA	NM_022712.3	*161*
ACSL4	F: CCATATCGC TCTGTC ACG CAC TTC R: CCAGGC TGTCCTTCTTCCCAAAC	NM_019370.2	200
β-Actin	F: CAGCCTTCCTTCTTGGGTATG R: AGCTCAGTAACAGTCCGCCT	NM_031144.3	360

Nrf2, nuclear factor erythroid 2–related factor 2; NF-κB, nuclear factor kappa B; GPX4, glutathione peroxidase 4; SLC7A11, solute carrier family 7 member 11; ACSL4, acyl-CoA synthetase long-chain family member 4; β-actin, beta-actin.

Histopathological Examination

Cardiac tissue samples from six rats per group (n = 6) were collected immediately after euthanasia and immersed in 10% neutral buffered formalin for 24 h. Following fixation, the specimens were processed using routine histological procedures, including dehydration through ascending concentrations of ethanol, clearing in xylene, and embedding in paraffin wax. Serial sections of 5 μm thickness were prepared and stained with hematoxylin and eosin (H&E). The stained sections were examined using a Leica DM500 light microscope (Leica Microsystems, Germany), and representative images were captured using a Leica ICC50 HD digital camera. For each animal, three H&E-stained sections were evaluated, with five non-overlapping microscopic fields examined per section, yielding 15 fields per animal. Histopathological alterations, including myocardial fiber degeneration/disorganization, cytoplasmic vacuolation, interstitial edema, inflammatory cell infiltration, and vascular congestion, were evaluated using a semiquantitative four-point severity scoring system adapted from previously described methods for experimental cardiotoxicity (Billingham et al. 1978) . Lesions were graded according to the approximate proportion of the examined field affected as follows: 0, absent; 1, mild (≤25%); 2, moderate (26–50%); and 3, severe (>50%). Scores obtained from the examined fields were averaged to generate a single animal-level histopathological severity score for statistical analysis. Sections were coded before examination, and all histopathological evaluations and scoring were performed by an investigator blinded to experimental group allocation.

Transmission Electron Microscopy (TEM)

Cardiac tissue samples from four rats per group (n=4) were collected immediately after dissection and fixed in cold 2.5% glutaraldehyde prepared in 0.1 M phosphate buffer (pH 7.4) for 24 h. Samples were washed several times with phosphate buffer and post-fixed in 1% osmium tetroxide for 2 h. The specimens were subsequently dehydrated through ascending concentrations of ethanol, transferred to acetone, and embedded in epoxy resin. Ultrathin sections (60–70 nm) were prepared using an ultramicrotome, mounted on copper grids, and double-stained with uranyl acetate and lead citrate. Sections were examined using a JEOL JEM-2100 transmission electron microscope (JEOL Ltd., Tokyo, Japan) operated at 160 kV. Representative electron micrographs were obtained to assess myofibrillar organization, mitochondrial morphology and integrity, and other treatment-associated ultrastructural alterations.

Isolation and Primary Culture of Adult Rat Ventricular Cardiomyocytes

Adult ventricular cardiomyocytes were isolated from male Wistar rats by enzymatic dissociation using retrograde Langendorff perfusion, based on the method described by Louch et al. (2011). Following deep anesthesia, hearts were rapidly excised and transferred to ice-cold physiological solution. The aorta was immediately cannulated, and the heart was mounted on a Langendorff apparatus and retrogradely perfused at 37 °C. The heart was initially perfused with oxygenated Ca^{2+}-free Krebs–Henseleit buffer to remove residual blood and facilitate calcium depletion, followed by perfusion with collagenase type II-containing digestion buffer until adequate softening of the ventricular tissue was achieved.

Following enzymatic digestion, the atria and visible connective tissues were removed, and the ventricular tissue was minced and gently triturated to release individual cardiomyocytes. The resulting cell suspension was filtered through a sterile nylon mesh, and cardiomyocytes were enriched by low-speed sedimentation to reduce contamination by non-myocyte cells. Extracellular Ca^{2+} was then gradually reintroduced to allow progressive calcium adaptation. The enriched cardiomyocytes were resuspended in cardiomyocyte culture medium supplemented with fetal bovine serum, penicillin–streptomycin, and the appropriate survival supplements, seeded onto laminin-coated culture plates, and maintained at 37 °C in a humidified atmosphere containing 5% CO_2. Following initial attachment, the medium was replaced with serum-reduced maintenance medium. Only preparations predominantly containing viable, rod-shaped cardiomyocytes with clearly visible cross-striations were used for subsequent experiments.

Experimental Design for Primary Cardiomyocytes

Preliminary concentration–response experiments were performed to identify non-cytotoxic concentrations of NOB and NOB-CHNPs and a DOX concentration producing reproducible but submaximal cardiomyocyte injury. Based on these preliminary experiments and previously established experimental models, the concentrations selected for the main experiment were 100 μM NOB, NOB-CHNPs containing an equivalent concentration of 100 μM NOB, and 1 μM DOX.

The primary experiment comprised eight groups: control, CHNPs, NOB (100 μM), NOB-CHNPs (equivalent to 100 μM NOB), DOX (1 μM), DOX (1 μM) + CHNPs, DOX (1 μM) + NOB (100 μM), and DOX (1 μM) + NOB-CHNPs (equivalent to 100 μM NOB). To provide pharmacological evidence for the contribution of Nrf2-, NF-κB-, and ferroptosis-related signaling, four additional groups were included: DOX + NOB-CHNPs + ML385 (5 μM; Nrf2 inhibitor), DOX + BAY 11-7082 (5 μM; NF-κB inhibitor), DOX + ferrostatin-1 (Fer-1; 1 μM; ferroptosis

inhibitor), and DOX + NOB-CHNPs + RSL3 (0.1 μM; GPX4 inhibitor/ferroptosis inducer). Thus, the complete in vitro experiment comprised 12 experimental groups.

ML385 and RSL3 were used to determine whether pharmacological disruption of Nrf2- and GPX4-associated signaling, respectively, attenuated the protection afforded by NOB-CHNPs. In parallel, BAY 11-7082 and Fer-1 were used to determine whether pharmacological inhibition of NF-κB-associated inflammatory signaling or ferroptosis-related processes reproduced components of the protective response. Cardiomyocytes were pretreated with the appropriate test formulation or pharmacological modulator before DOX challenge according to the experimental protocol. Concentrations were selected from preliminary concentration–response experiments and relevant literature to achieve pathway modulation while minimizing direct cytotoxicity. Untreated cardiomyocytes maintained under otherwise identical culture conditions served as controls. Six independent biological replicates were analyzed per experimental group.

Assessment of Cardiomyocyte Injury, Oxidative Stress, and Inflammation

Cardiomyocyte injury was evaluated by measuring LDH release into the culture supernatant using the LDH Assay Kit (Cytotoxicity; ab65393, Abcam, Cambridge, UK), according to the manufacturer's instructions. Intracellular ROS generation was determined using the DCFDA/H2DCFDA Cellular ROS Assay Kit (ab113851, Abcam) and measured fluorometrically at excitation/emission wavelengths of 485/535 nm, with ROS production expressed relative to the untreated control. Cellular lipid peroxidation was evaluated using the Lipid Peroxidation (MDA) Assay Kit (ab118970, Abcam), with MDA quantified at 532 nm and normalized to total cellular protein (nmol/mg protein). Inflammatory responses were assessed by measuring TNF-α and IL-6 in culture supernatants using rat-specific ELISA kits (TNF-α, ab100785; IL-6, ab100772; Abcam) according to the manufacturer's instructions. Cytokine concentrations were calculated from the corresponding standard curves and expressed as pg/mL. All assays were conducted using six biological replicates per experimental group (n=6).

Assessment of Lipid Peroxidation by C11-BODIPY 581/591 Flow Cytometry

Oxidation-sensitive C11-BODIPY 581/591 fluorescence was used to assess cellular lipid peroxidation as a ferroptosis-related endpoint. Following the experimental treatments, cardiomyocytes were incubated with C11-BODIPY 581/591 at a final concentration of 2 μM for 30 min at 37 °C in the dark. Cells were subsequently washed with phosphate-buffered saline and gently collected to minimize mechanical injury. Flow-cytometric analysis was performed using

488-nm excitation. Oxidation of C11-BODIPY 581/591 causes a fluorescence shift from the reduced red-emitting form toward the oxidized green-emitting form. After exclusion of debris and non-cellular events, at least 10,000 cellular events were acquired for each sample. Oxidized C11-BODIPY was quantified from the green fluorescence signal using a consistent analysis gate across experimental groups, and the results were expressed as the percentage of cells exhibiting oxidized C11-BODIPY fluorescence. Six biological replicates were analyzed per group (n=6).

The effects of Fer-1 and RSL3 were included as pharmacological controls to strengthen interpretation of the C11-BODIPY findings in relation to ferroptosis-associated lipid peroxidation. Because C11-BODIPY oxidation reflects lipid peroxidation rather than ferroptosis exclusively, these data were interpreted together with the effects of the ferroptosis modulators and the corresponding GPX4/SLC7A11/ACSL4-related findings.

Experimental Replication

All cellular experiments were performed using cardiomyocytes obtained from independent animals, with each independent isolation considered to be one biological replicate. Technical replicate wells from the same cardiomyocyte isolation were averaged before statistical analysis to avoid pseudoreplication. Investigators performing biochemical and flow-cytometric analyses were blinded to treatment allocation whenever feasible.

Statistical Analysis

All statistical procedures were performed using SAS software (Version 9.4; SAS Institute Inc., Cary, NC, USA). Before analysis, the data set was examined for distributional assumptions. Normality was evaluated using the Shapiro–Wilk test, while Levene's test was applied to assess the homogeneity of variances. Group differences were examined using one-way analysis of variance (ANOVA). Tukey's honestly significant difference (HSD) test was subsequently applied for pairwise comparisons when the overall ANOVA indicated statistical significance. Results are expressed as mean ± standard error of the mean (SEM). A probability value of $P < 0.05$ was considered statistically significant. Microsoft Excel was used for initial data organization, whereas GraphPad Prism version 9.0 (GraphPad Software, San Diego, CA, USA) was used to generate the graphical presentations.

Results:

Physicochemical Characteristics of NOB-CSNPs

The morphology and colloidal properties of the Nobiletin-Loaded Chitosan Nanoparticles **(**NOB-CHNPs) were examined by TEM and DLS (**Figure 1**). TEM imaging showed discrete nanoparticles with a mainly spherical morphology and clearly defined outlines (**Figure 1A**). The particles appeared well separated, with no marked aggregation. Most of the observed particles fell within the 82-117 nm size range (**Figure 1B**).

The hydrodynamic properties obtained by DLS showed a Z-average diameter of 136.03 nm (**Figure 1C**). The PDI was 0.255, indicating a relatively uniform particle population. The nanoparticles also exhibited a zeta potential of +53 mV (**Figure 1D**). This positive surface charge is consistent with the protonation of amino groups in chitosan. It may also promote electrostatic repulsion between nanoparticles and reduce their tendency to aggregate, thereby contributing to dispersion stability.

Encapsulation Efficiency and Drug Loading

The encapsulation efficiency (EE) of NOB in the prepared NOB-CHNPs was 89.46%, indicating efficient incorporation of NOB into the nanoparticle system. The corresponding drug loading capacity was 14.95%. The high EE% suggests that most of the initial NOB was successfully incorporated during nanoparticle preparation, with only a small fraction remaining unencapsulated.

In Vitro Sustained Release of NOB

The NOB-CHNPs showed a gradual release of NOB throughout the 48 h study period. Only a small fraction of the loaded NOB was released during the initial hours. The cumulative release reached 38.9% at 12 h and increased to 57.8% at 24 h. At 48 h, approximately 76.2% of the loaded NOB had been released (**Figure 2**). The gradual increase over time indicates a sustained release pattern from the chitosan nanoparticle matrix.

FTIR Spectral Analysis of NOB-CSNPs

FTIR spectroscopy was used to examine the chemical features of NOB, chitosan, and the NOB-CHNPs (**Figure 3**). The chitosan spectrum showed the characteristic broad O–H/N–H band around 3375 cm^{-1}. Other bands appeared near 2921, 1592, 1414, and 1072 cm^{-1}. NOB showed distinct bands associated with its carbonyl and aromatic groups. These included bands around 1658, 1606, 1512, and 1268 cm^{-1}. The spectrum of the NOB-CHNPs retained characteristic features of both components, although several bands showed changes in position

and intensity. The broad O–H/N–H band appeared around 3391 cm^{-1}. The NOB-associated band near 1658 cm^{-1} was observed at approximately 1639 cm^{-1} after nanoparticle formation. A change was also observed in the chitosan-related band near 1592 cm^{-1}. These shifts suggest interactions between NOB and the chitosan-based matrix during nanoparticle formation. The overall spectral profile, together with the high encapsulation efficiency and drug loading, supports the successful incorporation of NOB into the nanoparticles.

Stability of NOB-CHNPs During Storage

The NOB-CHNPs showed good physical stability during storage at 4°C for 30 days (**Table 2**). Particle size changed only slightly over the storage period. The PDI also remained relatively stable. No marked particle aggregation was observed. The zeta potential remained strongly positive throughout storage. This indicates that the surface characteristics of the nanoparticles were largely preserved. Overall, the formulation showed no signs of physical instability during the tested storage period

Table 2. Stability profile of NOB-CHNPs during storage at 4 °C for 30 days

Storage time	Particle size (nm)	PDI	Zeta potential (mV)
Day 0	136.03 ± 3.27	0.255 ± 0.012	+53.0 ± 1.84
Day 7	137.12 ± 3.01	0.257 ± 0.011	+52.6 ± 1.71
Day 14	138.20 ± 3.53	0.261 ± 0.013	+52.1 ± 1.96
Day 21	140.37 ± 3.62	0.264 ± 0.014	+51.4 ± 2.03
Day 30	141.19 ± 3.85	0.268 ± 0.015	+50.8 ± 2.10

Effect of NOB and NOB-CHNPs on Serum Cardiac Injury Biomarkers

Serum levels of troponin T (**Figure 4A**), CK-MB (**Figure 4B**), myoglobin (**Figure 4C**), and LDH (**Figure 4D**) were significantly increased in the DOX-treated group compared with the normal control group ($p<0.05$). Co-treatment with NOB and NOB-CHNPs reduced the levels of all measured cardiac injury biomarkers compared with the DOX-only group. The reductions in troponin T, CK-MB, myoglobin, and LDH were 47.78%, 44.48%, 56.13%, and 48.35%, respectively, in the DOX+NOB-CHNPs group, compared with 33.34%, 33.31%, 38.99%, and 31.83%, respectively, in the DOX+NOB group. Thus, the NOB-CHNPs group showed a greater reduction in all four biomarkers than the crude NOB group. No significant difference in serum myoglobin was detected between the DOX+NOB-CHNPs and normal control groups ($p>0.05$).

Treatment with empty chitosan nanoparticles did not significantly alter CK-MB, myoglobin, or LDH levels compared with the DOX-only group, whereas troponin T was significantly reduced in the DOX+CHNPs group.

Effect of NOB and NOB-CHNPs on Myocardial Antioxidant Defense

DOX exposure significantly reduced cardiac tissue levels of Nrf2 protein (**Figure 5A**), Nrf2 mRNA (**Figure 5B**), and heme oxygenase 1 (HO-1) protein (**Figure 5C**) vs. untreated control. Both NOB and NOB-CHNPs significantly increased these markers relative to DOX-treated animals. NOB-CHNPs treatment resulted in a more marked increase than crude NOB treatment. Compared with the DOX-only group, NOB-CHNPs increased Nrf2 protein, Nrf2 mRNA, and HO-1 protein levels by 82.90%, 210.00%, and 83.94%, respectively. The corresponding increases following crude NOB treatment were 45.08%, 132.22%, and 52.19%, respectively. No significant differences were detected between the DOX and DOX+CHNPs groups for Nrf2 protein or Nrf2 mRNA levels, whereas HO-1 protein was significantly increased in the DOX+CHNPs group.

In parallel, DOX exposure significantly decreased reduced glutathione (GSH) levels (**Figure 5D**), superoxide dismutase (SOD) (**Figure 5E**) and catalase (CAT) (**Figure 5F**) activity compared with the untreated control group. Co-treatment with NOB-CHNPs restored these parameters more effectively than crude NOB treatment. NOB-CHNPs increased GSH, SOD, and CAT by 186.48%, 105.35%, and 82.85%, respectively. Crude NOB increased these parameters by 136.91%, 61.59%, and 48.88%, respectively, relative to the DOX-only group. No significant differences were observed between the DOX+NOB-CHNPs and the normal control groups for GSH or SOD activity. In addition, CHNPs treatment significantly increased GSH levels compared with the DOX-only group, whereas no significant differences were detected between the DOX and DOX+CHNPs groups for SOD or CAT activities.

Effect of NOB and NOB-CHNPs on Oxidative Stress Biomarkers

DOX exposure significantly increased myocardial tissue levels of malondialdehyde (MDA), a biproduct of lipid peroxidation, (**Figure 5G**) and 8-hydroxy-2′-deoxyguanosine (8-OHdG), a biproduct of oxidative DNA damage, (**Figure 5H**) compared with the normal control group. Treatment with either NOB or NOB-CHNPs significantly reduced both of these oxidative stress biomarkers compared with the DOX-only group, with significantly lower levels observed in the DOX+NOB-CHNPs group than in the DOX+NOB group. Compared with the DOX-only group, MDA and 8-OHdG levels decreased by 48.54% and 37.41%, respectively, following NOB-CHNPs

treatment. Crude NOB produced reductions of only 32.79% and 26.52%, respectively. No significant difference in 8-OHdG levels was observed between the DOX and DOX+CHNPs groups, whereas MDA levels were marginally lower in the DOX+CHNPs group.

Effect of NOB and NOB-CHNPs on Myocardial Inflammation

Regarding the inflammatory response, DOX exposure significantly increased cardiac tissue NF-κB protein expression (**Figure 6A**) and NF-κB mRNA (**Figure 6B**) compared with the untreated control group. NOB and NOB-CHNPs significantly reduced both parameters compared with the DOX-only group. The DOX+NOB-CHNPs group showed a stronger reduction than the DOX+NOB group ($p<0.05$). NF-κB protein and mRNA levels decreased by 49.56% and 46.07%, respectively, in the DOX+NOB-CHNPs group, vs. 35.85% and 28.93%, respectively, in the DOX+NOB group relative to the DOX-only group. No significant difference was observed between the DOX+NOB-CHNPs and the untreated control groups for NF-κB mRNA levels ($p>0.05$). No significant differences were detected between the DOX and DOX+CHNPs groups for either NF-κB protein or mRNA levels.

Similarly, cardiac tissue levels of the pro-inflammatory cytokines TNF-α (**Figure 6C**), IL-6 (**Figure 6D**), and IL-1β (**Figure 6E**) were significantly increased in the DOX-treated group compared vs. the untreated control group. Co-treatment with NOB-CHNPs reduced these cytokines more effectively than crude NOB treatment. TNF-α, IL-6, and IL-1β levels decreased by 27.13%, 31.98%, and 44.84%, respectively, in the DOX+NOB-CHNPs group, compared with 14.60%, 23.73%, and 29.02%, respectively, in the DOX+NOB group, relative to the DOX-only group. IL-1β levels did not differ significantly between the DOX+NOB-CHNPs and normal control groups. Treatment with CHNPs alone did not decrease TNF-α or IL-6 significantly compared with the DOX-only group; whereas, IL-1β was somewhat reduced.

Effect of NOB and NOB-CHNPs on Mitochondrial Dysfunction

DOX exposure significantly decreased cardiac tissue levels of Sirtuin 1 (SIRT1) (**Figure 7A**), Peroxisome Proliferator-Activated Receptor Gamma Coactivator 1-Alpha (PGC-1α) (**Figure 7B**), and ATP Citrate Lyase (ACLY) (**Figure 7C**) compared with the normal control group. In contrast, cardiac tissue cytochrome c levels (**Figure 7D**) were significantly increased following DOX exposure. Co-treatment with NOB or NOB-CHNPs significantly improved these

mitochondrial dysfunction-related markers compared with the DOX-only group. The greater effects were observed in the DOX+NOB-CHNPs group. SIRT1, PGC-1α, and ACLY levels increased by 112.72%, 149.74%, and 121.46%, respectively, whereas cytochrome c decreased by 65.17% in the DOX+NOB-CHNPs group compared with the DOX-only group. In the DOX+NOB group, SIRT1, PGC-1α, and ACLY increased by 63.30%, 73.64%, and 78.03%, respectively, while cytochrome c decreased by 44.35%. No significant difference was observed between the DOX+NOB-CHNPs and normal control groups for cardiac PGC-1α levels. Treatment with CHNPs alone did not significantly affect SIRT1, ACLY, or cytochrome c levels compared with the DOX-only group, but PGC-1α was slightly increased.

Effect of NOB and NOB-CHNPs on Apoptotic Markers

DOX exposure significantly increased cardiac tissue levels of the pro-apoptotic markers Bax (**Figure 8A**) and caspase-3 (**Figure 8B**) compared with the untreated control group. NOB and NOB-CHNPs significantly reduced these levels compared with DOX alone. The reduction was more pronounced in the DOX+NOB-CHNPs group than in the DOX+NOB group. Bax and caspase-3 levels decreased by 40.10% and 38.35%, respectively, in the DOX+NOB-CHNPs group, compared with 26.90% and 24.44%, respectively, in the DOX+NOB group relative to the DOX-only group. In contrast, DOX exposure significantly decreased the cardiac tissue level of the anti-apoptotic marker Bcl-2 (**Figure 8C**) compared with the untreated control group. Co-treatment with NOB-CHNPs increased Bcl-2 levels more effectively than crude NOB, restoring them to values that did not significantly differ from those of the untreated control group. Bcl-2 increased by 91.34% in the DOX+NOB-CHNPs group compared with 43.31% in the DOX+NOB group relative to the DOX-only group. No significant differences were observed between the DOX and DOX+CHNPs groups for any of the assessed pro- or anti-apoptotic markers.

Effect of NOB and NOB-CHNPs on Ferroptosis Markers

DOX exposure significantly increased cardiac tissue iron content (**Figure 9A**) and markers of ferroptosis: Acyl-CoA synthetase long-chain family member 4 (ACSL4) protein (**Figure 9B**), ACSL4 mRNA (**Figure 9C**), and lipid peroxidation (LPO) (**Figure 9D**) compared with the nontreated control group. NOB and NOB-CHNPs significantly reduced these parameters compared with DOX alone. The DOX+NOB-CHNPs group showed larger reductions than the DOX+NOB group. Iron content, ACSL4 protein, ACSL4 mRNA, LPO, and 4-hydroxynonenal (4-HNE) levels decreased by 49.52%, 44.36%, 54.20%, 60.02%, and 44.63%, respectively, in the

DOX+NOB-CHNPs group, compared with 31.43%, 27.22%, 22.70%, 37.40%, and 28.89%, respectively, in the DOX+NOB group relative to the DOX-only group. No significant difference in LPO levels was observed between the DOX+NOB-CHNPs and nontreated control groups.

In contrast, DOX exposure significantly decreased cardiac tissue levels of the anti-ferroptotic markers glutathione peroxidase 4 (GPX4) protein (**Figure 9E**), GPX4 mRNA (**Figure 9F**), solute carrier family 7 member 11 (SLC7A11) protein (**Figure 9G**), and SLC7A11 mRNA (**Figure 9H**) compared with the normal control group. Treatment with NOB or NOB-CHNPs significantly increased these markers compared with the DOX-only group. The increases were more pronounced following NOB-CHNPs treatment than crude NOB treatment. GPX4 protein, GPX4 mRNA, SLC7A11 protein, and SLC7A11 mRNA increased by 227.39%, 159.00%, 178.58%, and 115.13%, respectively, in the DOX+NOB-CHNPs group, compared with 103.79%, 93.87%, 104.63%, and 77.49%, respectively, in the DOX+NOB group relative to the DOX-only group. No significant difference in GPX4 mRNA levels was observed between the DOX+NOB-CHNPs and normal control groups. Treatment with CHNPs alone did not significantly alter the assessed pro- or anti-ferroptotic markers compared with the DOX-only group, except for iron content, GPX4 protein, and GPX4 mRNA levels.

Effect of NOB and NOB-CHNPs on DOX-Induced Cardiac Histopathological Changes

The cardiac sections from the control and treatment groups are shown in **Figure 10**. Myocardial tissue from the nontreated animals showed the expected normal histological appearance, with orderly cardiomyocyte arrangement, centrally positioned vesicular nuclei, distinct striations and Z-bands. A comparable appearance was observed in the CHNPs, free NOB, and NOB-CHNPs groups (**Figure 10A–D**), with preserved myocardial fibers and interstitial spaces and no apparent degenerative or inflammatory changes.

A distinctly different pattern was observed following DOX administration (**Figure 10E**). The myocardial architecture was severely disrupted, with irregularly arranged cardiomyocytes, cytoplasmic vacuolation, myofibrillar degeneration, areas of myocytolysis, prominent loss of cross-striations, interstitial edema, inflammatory cell infiltration, and vascular congestion.
Several cardiomyocytes also exhibited pyknotic nuclei. Administration of empty CHNPs to DOX-treated rats produced only limited morphological improvement (**Figure 10F**), with focal degenerative changes, vacuolation, edema, and inflammatory infiltration remaining evident. In contrast, administration of free NOB treatment markedly preserved myocardial architecture

(**Figure 10G**), as evidenced by more regularly arranged cardiomyocytes, reduced vacuolar and degenerative changes, better preservation of cross-striations, and less inflammatory infiltration. These effects were further amplified in the DOX + NOB-CHNPs group (**Figure 10H**), in which most myocardial fibers showed near-normal organization, preserved cross-striations and centrally located nuclei, with only minor residual interstitial and inflammatory alterations. Semiquantitative histopathological scoring supported these microscopic observations (**Figure 10I**). The control, CHNPs, NOB, and NOB-CHNPs groups exhibited low severity scores (0.17, 0.20, 0.13, and 0.12, respectively), with no significant differences among these groups (all $p \geq 0.9901$). DOX markedly increased the histopathological severity score to 2.63 compared with the control ($p<0.0001$). Empty CHNPs did not significantly attenuate this increase (2.50; $p = 0.8725$ vs. DOX). In contrast, free NOB significantly reduced the severity score to 1.48 ($p<0.0001$ vs. DOX), while NOB-CHNPs produced a greater reduction to 0.72 ($p<0.0001$ vs. DOX). Importantly, the score in the DOX + NOB-CHNPs group was significantly lower than that in the DOX + NOB group (mean difference, 0.76; $p<0.0001$), supporting greater histological preservation with NOB-CHNPs than with free NOB.

Effect of NOB and NOB-CHNPs on DOX-Induced Cardiac Ultrastructural Alterations

Transmission electron microscopy revealed clear differences in myocardial ultrastructure among the experimental groups (**Figure 11A–H**). Cardiomyocytes from the control, chitosan, free NOB, and NOB-CHNPs groups (**Figure 11A–D**) maintained a normal ultrastructural appearance. The myofibrils were regularly arranged, with preserved Z-lines and intact oval nuclei. Mitochondria were abundant and showed well-defined cristae and preserved matrix density. In contrast, DOX exposure caused marked disruption of the myocardial ultrastructure (**Figure 11E**). The cardiomyocytes showed disorganized myofibrils with focal Z-line disruption. Mitochondria appeared swollen and exhibited structural damage, including loss and fragmentation of cristae. The DOX-treated rats receiving chitosan showed a partial improvement in myocardial morphology (**Figure 11F**). Compared with the DOX group, myofibrillar organization was better preserved, while mitochondrial swelling and intracellular lipid accumulation were less pronounced. However, many focal abnormalities remained, indicating incomplete protection by chitosan alone. Administration of free NOB to DOX-exposed rats produced a more evident improvement in cardiac ultrastructure (**Figure 11G**). The myofibrils showed better alignment and preservation of Z-lines. Mitochondrial morphology was also improved, with fewer swollen mitochondria and

better-preserved cristae. The most pronounced structural recovery was observed in the DOX + NOB-CHNPs group (**Figure 11H**). Cardiomyocytes largely retained their normal organization, with well-preserved myofibrils, distinct Z-lines, and intact nuclei. Mitochondria exhibited preserved shape, matrix density, and cristae architecture, with minimal evidence of swelling or structural disruption.

Effect of NOB and NOB-CHNPs on Markers of Inflammation and Oxidative Stress in Cultured Cardiac Myocytes

Results from primary cultures of isolated cardiac myocytes further supported the involvement of Nrf2-, NF-κB-, and ferroptosis-related signaling in the protective effects of NOB-CHNPs against DOX-induced cardiomyocyte injury. DOX markedly increased LDH release (**Figure 12A**), ROS (**Figure 12B**), MDA (**Figure 12C**), TNF-α (**Figure 12D**), and IL-6 (**Figure 12E**), whereas NOB-CHNPs significantly attenuated these alterations and generally exerted greater effects than free NOB (all $p < 0.0001$ vs. DOX). Mechanistically, Nrf2 inhibition with ML385 significantly diminished NOB-CHNP-mediated protection, increasing LDH, ROS, MDA, TNF-α, and IL-6 by approximately 1.55-, 1.61-, 1.64-, 1.64-, and 1.60-fold, respectively, relative to NOB-CHNPs alone (all $p < 0.0001$). NF-κB inhibition with BAY 11-7082 significantly reduced DOX-induced LDH, ROS, MDA, TNF-α, and IL-6, with marked suppression of the inflammatory cytokines TNF-α and IL-6 to approximately 0.49- and 0.46-fold of DOX values, respectively (both $p<0.0001$). Ferroptosis inhibitor ferrostatin-1 (Fer-1) similarly attenuated DOX-induced cellular injury and oxidative alterations, whereas GPX4 inhibition with RSL3 reversed NOB-CHNP-mediated protection, increasing LDH, ROS, MDA, TNF-α, and IL-6 by approximately 1.48-, 1.68-, 1.73-, 1.54-, and 1.53-fold, respectively ($p<0.0001$ vs. NOB-CHNPs). Collectively, these pharmacological intervention findings support contributions of Nrf2-dependent antioxidant signaling, NF-κB-associated inflammatory responses, and GPX4-related ferroptosis regulation to the protective effects of NOB-CHNPs.

Flowcytometry showed that DOX exposure markedly increased lipid peroxidation (assessed by C11-BODIPY oxidation) from 5.42% in control cells to 48.0% ($p<0.0001$), whereas CHNPs did not significantly modify the DOX-induced increase (44.0%; $p=0.2795$ vs. DOX). Free NOB significantly reduced C11-BODIPY oxidation to 20.67%, while NOB-CHNPs produced a greater reduction to 9.83% (both $p<0.0001$ vs. DOX; NOB vs. NOB-CHNPs, $p<0.0001$). Notably, C11-BODIPY oxidation following NOB-CHNP treatment did not differ significantly from the

control (p=0.1822). Fer-1 similarly reduced C11-BODIPY oxidation to 10.67% (p<0.0001 vs. DOX), with no significant difference from either NOB-CHNPs (p=0.9990) or the control (p=0.0671). In contrast, RSL3 (GPX4 inhibitor) markedly attenuated the effect of NOB-CHNPs, increasing C11-BODIPY oxidation to 36.0% (p<0.0001 vs. DOX + NOB-CHNPs). These pharmacological findings support the protective effect of NOB-CHNPs on GPX4-mediated regulation of lipid peroxidation (**Figure 13**).

Discussion

Treatment with DOX resulted in obvious cardiac injury, as indicated by increased markers of cardiac injury together with oxidative stress, inflammation, mitochondrial dysfunction, apoptosis, ferroptosis, and structural myocardial damage. Both free NOB and NOB-CHNPs attenuated these abnormalities, with NOB-CHNPs generally producing greater effects. Importantly, the present findings extend previous evidence for the cardioprotective activity of free NOB by demonstrating that chitosan nanoencapsulation was associated with greater protection at an equivalent NOB dose and by integrating oxidative, inflammatory, mitochondrial, apoptotic, and ferroptosis-related endpoints. Results from isolated cardiomyocyte provide further evidence supporting the contribution of Nrf2-, NF-κB-, and GPX4-mediated mechanisms. Because pharmacokinetics and cardiac tissue concentrations of NOB were not measured, however, the greater efficacy of NOB-CHNPs cannot be attributed directly to improved bioavailability or myocardial delivery.

The increases in circulating cardiac troponin, CK-MB, LDH, and myoglobin following DOX administration were consistent with myocardial injury and loss of cardiomyocyte integrity (Netala et al. 2025). This pattern agrees with previous experimental evidence demonstrating that cumulative DOX exposure induces cardiomyocyte injury through interconnected oxidative, mitochondrial, and cell-death processes (Bhutani et al. 2025; Osataphan et al. 2020). Both NOB formulations reduced these cardiac injury markers, with NOB-CHNPs exerting greater effects than free NOB. These observations are consistent with the cardioprotective effects of NOB previously reported in DOX-induced cardiac injury (Sunagawa et al. 2025); however, the direct comparison at an equivalent NOB dose indicates a marked additional benefit of the nanoparticle formulation, which is a significant novel contribution of this study.

Oxidative stress represents a major component of DOX-mediated cardiotoxicity. DOX undergoes redox cycling and disrupts mitochondrial function, thereby promoting ROS generation and oxidative damage to cellular macromolecules (Aryal and Rao 2016; Qiu et al. 2025). Consistent with this mechanism, DOX increased ROS, MDA, and 8-OHdG while decreasing GSH, SOD, and CAT, indicating enhanced lipid and DNA oxidation accompanied by impaired antioxidant defenses. NOB alone attenuated these alterations, but nanoparticle encapsulation (NOB-CHNPs) produced significantly greater effects. Previous studies have similarly demonstrated antioxidant effects of NOB in experimental tissue injury, including DOX-associated oxidative damage (Atila Uslu et al. 2025; Çetinkaya et al. 2026). Thus, the present findings support enhanced preservation of redox homeostasis with NOB-CHNPs through formulation-dependent increase in NOB bioavailability.

The oxidative changes were accompanied by alterations in Nrf2/HO-1 signaling. Nrf2 is an important regulator of cellular antioxidant defense and controls the expression of cytoprotective proteins, including HO-1 (Wu et al. 2022). DOX decreased Nrf2 and HO-1, whereas both NOB treatments attenuated these changes, with a greater response to NOB-CHNPs. These associations suggest that preservation of Nrf2/HO-1 signaling may contribute to the antioxidant effects of NOB-CHNPs. This interpretation is strengthened by findings from isolated cardiomyocytes, in which the Nrf2 inhibitor, ML385, attenuated NOB-CHNP-mediated protection and increased LDH release as well as additional oxidative stress and inflammatory indices relative to NOB-CHNP treatment.

Inflammation is another prominent component of DOX-induced myocardial injury. Increased NF-κB p65, TNF-α, IL-1β, and IL-6 in DOX-treated animals are consistent with an enhanced inflammatory response and with the recognized interaction between oxidative stress and NF-κB-associated signaling in DOX cardiotoxicity (Pang et al. 2021; Vitale et al. 2024). NOB and, more significantly NOB-CHNPs attenuated these alterations, consistent with previous evidence for the anti-inflammatory activity of NOB (Murata et al. 2023). Pharmacological inhibition of NF-κB with BAY 11-7082 also reduced DOX-induced cellular injury and inflammatory mediators in isolated cardiomyocytes, providing complementary support for the involvement of NF-κB-associated inflammatory signaling. Taken together with the effects of Nrf2 inhibition, these observations suggest that modulation of interconnected redox and inflammatory responses contributes to NOB-CHNP-mediated cardioprotection.

Mitochondrial dysfunction provided a further and functionally important link between oxidative injury, myocardial metabolism and myocardial injury. Treatment with DOX decreased SIRT1, PGC-1α, and ATP and increased cytochrome *c*, indicating disruption of mitochondrial homeostasis and energy metabolism. SIRT1 and PGC-1α contribute to mitochondrial biogenesis and oxidative metabolism, whereas mitochondrial injury can promote cytochrome *c* release and subsequent initiation of the apoptotic cascade (Bayir and Kagan 2008; Chen et al. 2025). NOB attenuated these changes to an extent, but these effects were significantly greater in the NOB-CHNP-treated animals. The biochemical findings are supported by TEM, which demonstrated near complete preservation of mitochondrial morphology and cristae integrity following NOB-CHNP treatment. Thus, the molecular and ultrastructural findings collectively suggest preservation of mitochondrial homeostasis.

Consistent with mitochondrial involvement, DOX treatment increased Bax and caspase-3 and decreased Bcl-2, supporting enhanced pro-apoptotic signaling. Alteration of the Bax/Bcl-2 balance can favor mitochondrial membrane permeabilization, cytochrome *c* release, and downstream caspase activity (Czabotar and Garcia-Saez 2023). Both NOB formulations attenuated these alterations, with greater effects observed for NOB-CHNPs. These findings agree with (Sunagawa et al. 2025), who reported attenuation of DOX-induced cardiomyocyte apoptosis by NOB, and with previous studies demonstrating anti-apoptotic effects of NOB in other cardiac injury models (Liu et al. 2021). The present study therefore confirms apoptosis-related protection while extending the investigation to additional mechanisms implicated in DOX cardiotoxicity.

A particularly relevant extension of the present study was the evaluation of ferroptosis-related processes. DOX increased cardiac iron, lipid peroxidation, 4-HNE, and ACSL4 while decreasing GPX4 and SLC7A11. This pattern is consistent with increased susceptibility to iron-dependent lipid peroxidation, because GPX4 limits lipid hydroperoxide accumulation, SLC7A11 supports cystine uptake and glutathione-dependent antioxidant defense, and ACSL4 facilitates incorporation of polyunsaturated fatty acids into membrane phospholipids susceptible to oxidation (Kalinina 2026; Liu et al. 2021). NOB-CHNPs attenuated these changes more effectively than free NOB. Previous studies have implicated NOB in the modulation of ferroptosis in myocardial ischemia-reperfusion and other experimental injury models (Huang et al. 2023a; Huang et al. 2023b). The current findings extend these observations to DOX-induced cardiac injury and suggest involvement of the ACSL4/GPX4/SLC7A11-associated ferroptotic machinery.

Importantly, the cardiomyocyte experiments provided functional pharmacological support for this interpretation. DOX markedly increased an indicator of lipid peroxidation (C11-BODIPY oxidation), whereas NOB-CHNPs reduced it from 48.0% to 9.83% ($p < 0.0001$), an effect comparable to that of Fer-1, which is a direct inhibitor of lipid peroxidation (10.67%; $p = 0.9990$ vs. NOB-CHNPs). Conversely, GPX4 inhibition with RSL3 increased C11-BODIPY oxidation to 36.0% ($p < 0.0001$ vs. NOB-CHNPs) and attenuated other protective responses. The ability of Fer-1 to reproduce key protective effects and RSL3 to diminish NOB-CHNP-mediated protection provides stronger evidence for GPX4-related regulation of lipid peroxidation than measurement of ferroptosis-associated markers alone.

The molecular findings were consistent with the myocardial structural changes. DOX treatment caused marked cardiomyocyte degeneration, cytoplasmic vacuolation, myofibrillar disorganization, interstitial edema, and inflammatory cell infiltration, accompanied by myofibrillar disruption and mitochondrial swelling with loss of cristae integrity. Semiquantitative histopathological scoring supported these observations: empty CHNPs did not significantly reduce DOX-induced injury, whereas free NOB significantly decreased the severity score and NOB-CHNPs produced a further significant reduction compared with free NOB. The greater histological and ultrastructural preservation with NOB-CHNPs was therefore consistent with the biochemical and molecular findings. Notably, the absence of substantial protection with empty CHNPs indicates that the observed effects cannot be explained by the chitosan carrier alone under the present experimental conditions.

Taken together, the findings indicate that NOB-CHNPs provide greater protection than an equivalent dose of free NOB against experimental DOX-induced cardiac injury. Rather than reflecting a single pathway, this protection appears to involve interconnected preservation of redox homeostasis, Nrf2-associated antioxidant defenses, attenuation of NF-κB-associated inflammation, maintenance of mitochondrial integrity, modulation of apoptotic signaling, and limitation of GPX4-related lipid peroxidation. Results from isolated cardiomyocytes strengthen the mechanistic interpretation of the Nrf2-, NF-κB-, and ferroptosis-related observations obtained in vivo.

Study Limitations

Several limitations should be considered when interpreting these findings. First, only male rats were studied; therefore, potential sex-dependent differences in DOX cardiotoxicity and responses to NOB-CHNPs were not addressed. Second, pharmacokinetic parameters, circulating NOB concentrations, and cardiac tissue distribution were not measured. Consequently, the greater efficacy of NOB-CHNPs cannot be attributed directly to enhanced myocardial delivery. Third, although the study assessed multiple biochemical, molecular, histological, and ultrastructural endpoints, direct functional cardiac measurements, such as echocardiographic indices of ventricular function, were not performed. Fourth, the mechanistic cardiomyocyte experiments used pharmacological inhibitors and modulators, which may have off-target effects; genetic manipulation of Nrf2, NF-κB, GPX4, or related pathway components would provide additional mechanistic specificity. Finally, the relatively short experimental period models subacute cumulative DOX cardiotoxicity and does not establish whether the protective effects of NOB-CHNPs persist in chronic or delayed cardiomyopathy. These limitations support further investigation incorporating both sexes, pharmacokinetic and tissue-distribution analyses, functional cardiac assessment, longer follow-up, and complementary genetic pathway validation.

Conclusion

The present study demonstrates that DOX-induced cardiotoxicity is associated with oxidative stress, inflammation, mitochondrial dysfunction, apoptosis, and ferroptosis-related alterations. Both free NOB and NOB-CHNPs attenuated these changes, but NOB-CHNPs provided significantly greater biochemical, molecular, histopathological, and ultrastructural protection at an equivalent NOB dose. The integrated in vivo findings support the involvement of Nrf2/HO-1-associated antioxidant defense, NF-κB-associated inflammatory signaling, preservation of mitochondrial homeostasis, modulation of apoptotic responses, and regulation of AGPX4/SLC7A11-associated ferroptotic processes. Complementary cardiomyocyte experiments further supported the contributions of Nrf2, NF-κB, and GPX4-related ferroptosis mechanisms to NOB-CHNP-mediated cardioprotection. Collectively, these findings indicate that chitosan nanoencapsulation augments NOB-mediated cardioprotection against experimental DOX-induced cardiac injury and provide mechanistic support linking this protection to coordinated regulation of redox, inflammatory, mitochondrial, apoptotic, and ferroptosis-related processes. Further studies incorporating pharmacokinetic and cardiac distribution analyses, in vivo cardiac functional

assessment, longer-term models, and complementary mechanistic approaches are needed to determine the translational relevance of NOB-CHNPs.

Declarations:

Animal Ethics and Consent to Participate declarations: The animal study protocol was approved by the Institutional Animal Care and Use Committee of Mansoura University (MU-ACUC, VM.R.26.09.29; 11/4/2026). All procedures were carried out in accordance with Directive 2010/63/EU and the ARRIVE guidelines 2.0.

Consent to participate

Not applicable

Consent for publication

Not applicable

Availability of data and materials

The data supporting the findings of this study are available from the corresponding author upon reasonable request. No publicly archived datasets are applicable.

Competing interest

The authors declare that there is no conflict of interest related to the published manuscript.

Funding: The authors extend their appreciation to Northern Border University, Saudi Arabia, for supporting this work through project number (NBU-CRP-2027-2510).

Authors contribution

Conceptualization, E.M.E. and A.A.F.; methodology, E.M.E., M.M.M., E.E., and H.R.M.; validation, T.G.K., O.A.H., and P.R.; formal analysis, E.M.E., M.M.M., and O.A.H.; investigation, A.A.F., E.E., H.R.M., and T.G.K.; data curation, E.M.E., O.A.H., and P.R.; writing—original draft preparation, E.M.E., A.A.F., and M.M.M.; writing—review and editing, E.E., H.R.M., T.G.K.,

O.A.H., and P.R.; visualization, M.M.M. and O.A.H.; supervision, E.M.E. and P.R. All authors have read and agreed to the published version of the manuscript.

Clinical trial number: Not applicable

References:

Aguilera A, Berdun F, Bartoli C, Steelheart C, Alegre M, Bayir H, Tyurina YY, Kagan VE, Salerno G, Pagnussat G, Martin MV. C-ferroptosis is an iron-dependent form of regulated cell death in cyanobacteria. J Cell Biol. 2022;221. https://doi.org/10.1083/jcb.201911005

Arafa MH, Mohammad NS, Atteia HH, Abd-Elaziz HR. Protective effect of resveratrol against doxorubicin-induced cardiac toxicity and fibrosis in male experimental rats. J Physiol Biochem. 2014;70:701-11. https://doi.org/10.1007/s13105-014-0339-y

Aryal B, Rao VA. Deficiency in Cardiolipin Reduces Doxorubicin-Induced Oxidative Stress and Mitochondrial Damage in Human B-Lymphocytes. PLoS One. 2016;11:e0158376. https://doi.org/10.1371/journal.pone.0158376

Atila Uslu G, Uslu H, Çoban TA, Özkaraca M, Mendil AS, Aygörmez S. Nobiletin reduces 5-FU-induced lung injury with antioxidative, anti-inflammatory and anti-apoptotic activities. Naunyn Schmiedebergs Arch Pharmacol. 2025;398:8543-54. https://doi.org/10.1007/s00210-024-03773-6

Bashir SM, Ahmed Rather G, Patrício A, Haq Z, Sheikh AA, Shah M, Singh H, Khan AA, Imtiyaz S, Ahmad SB, Nabi S, Rakhshan R, Hassan S, Fonte P. Chitosan Nanoparticles: A Versatile Platform for Biomedical Applications. Materials (Basel). 2022;15. https://doi.org/10.3390/ma15196521

Bayir H, Kagan VE. Bench-to-bedside review: Mitochondrial injury, oxidative stress and apoptosis--there is nothing more practical than a good theory. Crit Care. 2008;12:206. https://doi.org/10.1186/cc6779

Belger C, Abrahams C, Imamdin A, Lecour S. Doxorubicin-induced cardiotoxicity and risk factors. Int J Cardiol Heart Vasc. 2024;50:101332. https://doi.org/10.1016/j.ijcha.2023.101332

Bhutani V, Varzideh F, Wilson S, Kansakar U, Jankauskas SS, Santulli G. Doxorubicin-Induced Cardiotoxicity: A Comprehensive Update. J Cardiovasc Dev Dis. 2025;12. https://doi.org/10.3390/jcdd12060207

Billingham ME, Mason JW, Bristow MR, Daniels JR. Anthracycline cardiomyopathy monitored by morphologic changes. Cancer Treat Rep. 1978;62:865-72.

Çetinkaya S, Süntar İ, Demirel MA, Çınar Ayan İ, Akarca Dizakar Ö. Nobiletin Ameliorates Doxorubicin-Induced Nephrotoxicity by Targeting Oxidative Stress, Inflammatory, and Apoptotic Pathways: Combined In Vivo and In Silico Insights. ACS Omega. 2026;11:7165-77. https://doi.org/10.1021/acsomega.5c07049

Chen J, Liu B, Yao X, Yang X, Sun J, Yi J, Xue F, Zhang J, Shen Y, Chen B, Sun H. AMPK/SIRT1/PGC-1α Signaling Pathway: Molecular Mechanisms and Targeted Strategies From Energy Homeostasis Regulation to Disease Therapy. CNS Neurosci Ther. 2025;31:e70657. https://doi.org/10.1111/cns.70657

Czabotar PE, Garcia-Saez AJ. Mechanisms of BCL-2 family proteins in mitochondrial apoptosis. Nat Rev Mol Cell Biol. 2023;24:732-48. https://doi.org/10.1038/s41580-023-00629-4

El-Saadony MT, Saad AM, Sitohy M, Alkafaas SS, Dladla M, Ghosh S, Mohammed DM, Soliman TN, Ibrahim EH, Fahmy MA, AbuQamar JS, El-Tarabily KA. Chitosan nanoparticles: Green synthesis, biological activities, and sustainable frontiers in targeted drug delivery and cancer nanomedicine - A comprehensive review. Mater Today Bio. 2025;35:102358. https://doi.org/10.1016/j.mtbio.2025.102358

Huang Q, Tian L, Zhang Y, Qiu Z, Lei S, Xia ZY. Nobiletin alleviates myocardial ischemia-reperfusion injury via ferroptosis in rats with type-2 diabetes mellitus. Biomed Pharmacother. 2023a;163:114795. https://doi.org/10.1016/j.biopha.2023.114795

Huang W, Chen H, He Q, Xie W, Peng Z, Ma Q, Huang Q, Chen Z, Liu Y. Nobiletin protects against ferroptosis to alleviate sepsis-associated acute liver injury by modulating the gut microbiota. Food Funct. 2023b;14:7692-704. https://doi.org/10.1039/d3fo01684f

Ju SN, Shi HH, Yang JY, Zhao YC, Xue CH, Wang YM, Huang QR, Zhang TT. Characterization, stability, digestion and absorption of a nobiletin nanoemulsion using DHA-enriched phosphatidylcholine as an emulsifier in vivo and in vitro. Food Chem. 2022;397:133787. https://doi.org/10.1016/j.foodchem.2022.133787

Kalinina E. GSH-Related Enzymes GPx4, Chac1, and GSTs and Redox Regulation of Ferroptosis in Cancer. Int J Mol Sci. 2026;27. https://doi.org/10.3390/ijms27146353

Katus HA, Remppis A, Neumann FJ, Scheffold T, Diederich KW, Vinar G, Noe A, Matern G, Kuebler W. Diagnostic efficiency of troponin T measurements in acute myocardial infarction. Circulation. 1991;83:902-12. https://doi.org/10.1161/01.cir.83.3.902

Kong CY, Guo Z, Song P, Zhang X, Yuan YP, Teng T, Yan L, Tang QZ. Underlying the Mechanisms of Doxorubicin-Induced Acute Cardiotoxicity: Oxidative Stress and Cell Death. Int J Biol Sci. 2022;18:760-70. https://doi.org/10.7150/ijbs.65258

Kuskov AN, Kukovyakina EV, Krasnoselskaya EN. Nanotechnology-Based Drug Delivery Systems. Pharmaceutics. 2025;17. https://doi.org/10.3390/pharmaceutics17070817

Li Y, Liu C, Fang B, Chen X, Wang K, Xin H, Wang K, Yang SM. Ferroptosis, a therapeutic target for cardiovascular diseases, neurodegenerative diseases and cancer. J Transl Med. 2024;22:1137. https://doi.org/10.1186/s12967-024-05881-6

Liu Z, Gao Z, Zeng L, Liang Z, Zheng D, Wu X. Nobiletin ameliorates cardiac impairment and alleviates cardiac remodeling after acute myocardial infarction in rats via JNK regulation. Pharmacol Res Perspect. 2021;9:e00728. https://doi.org/10.1002/prp2.728

Livak KJ, Schmittgen TD. Analysis of relative gene expression data using real-time quantitative PCR and the 2− ΔΔCT method. methods. 2001;25:402-8.

Louch WE, Sheehan KA, Wolska BM. Methods in cardiomyocyte isolation, culture, and gene transfer. J Mol Cell Cardiol. 2011;51:288-98. https://doi.org/10.1016/j.yjmcc.2011.06.012

Matsuzaki K, Ohizumi Y. Beneficial Effects of Citrus-Derived Polymethoxylated Flavones for Central Nervous System Disorders. Nutrients. 2021;13. https://doi.org/10.3390/nu13010145

Murata T, Ishiwa S, Lin X, Nakazawa Y, Tago K, Funakoshi-Tago M. The citrus flavonoid, nobiletin inhibits neuronal inflammation by preventing the activation of NF-κB. Neurochem Int. 2023;171:105613. https://doi.org/10.1016/j.neuint.2023.105613

Netala VR, Hou T, Wang Y, Zhang Z, Teertam SK. Cardiovascular Biomarkers: Tools for Precision Diagnosis and Prognosis. Int J Mol Sci. 2025;26. https://doi.org/10.3390/ijms26073218

Osataphan N, Phrommintikul A, Chattipakorn SC, Chattipakorn N. Effects of doxorubicin-induced cardiotoxicity on cardiac mitochondrial dynamics and mitochondrial function: Insights for future interventions. J Cell Mol Med. 2020;24:6534-57. https://doi.org/10.1111/jcmm.15305

Pang Y, Wu D, Ma Y, Cao Y, Liu Q, Tang M, Pu Y, Zhang T. Reactive oxygen species trigger NF-κB-mediated NLRP3 inflammasome activation involvement in low-dose CdTe QDs

exposure-induced hepatotoxicity. Redox Biol. 2021;47:102157. https://doi.org/10.1016/j.redox.2021.102157

Qiu Y, Chang S, Zeng Y, Wang X. Advances in Mitochondrial Dysfunction and Its Role in Cardiovascular Diseases. Cells. 2025;14. https://doi.org/10.3390/cells14201621

Rahaeng K, Oraintara A, Mahakham W. A Simple Ionic-Gelation Method for Chitosan Nanoparticle Synthesis and Standardized Protocols for Biological Safety Assessment: Antibacterial Activity, Phytotoxicity, and Biocompatibility. Int J Mol Sci. 2026;27. https://doi.org/10.3390/ijms27083673

Sharma S, Parashar M, Lal K, Naik M, Tanwar SS. Doxorubicin-Induced Cardiotoxicity: Comprehensive Pathway Insights and Advanced Preclinical Therapeutics. J Appl Toxicol. 2026;46:1801-37. https://doi.org/10.1002/jat.70131

Sunagawa Y, Iwashimizu S, Ono M, Mochizuki S, Iwashita K, Sato R, Shimizu S, Funamoto M, Shimizu K, Hamabe-Horiike T, Katanasaka Y, Murakami A, Asakawa T, Inai M, Kan T, Komiyama M, Hawke P, Mori K, Arakawa Y, Hasegawa K, Sakamoto K, Kurokawa J, Morimoto T. The citrus flavonoid nobiletin prevents the development of doxorubicin-induced heart failure by inhibiting apoptosis. J Pharmacol Sci. 2025;158:84-94. https://doi.org/10.1016/j.jphs.2025.03.011

Tomou EM, Papakyriakopoulou P, Skaltsa H, Valsami G, Kadoglou NPE. Bio-Actives from Natural Products with Potential Cardioprotective Properties: Isolation, Identification, and Pharmacological Actions of Apigenin, Quercetin, and Silibinin. Molecules. 2023;28. https://doi.org/10.3390/molecules28052387

Ulmer BM, Stoehr A, Schulze ML, Patel S, Gucek M, Mannhardt I, Funcke S, Murphy E, Eschenhagen T, Hansen A. Contractile Work Contributes to Maturation of Energy Metabolism in hiPSC-Derived Cardiomyocytes. Stem Cell Reports. 2018;10:834-47. https://doi.org/10.1016/j.stemcr.2018.01.039

Vitale R, Marzocco S, Popolo A. Role of Oxidative Stress and Inflammation in Doxorubicin-Induced Cardiotoxicity: A Brief Account. Int J Mol Sci. 2024;25. https://doi.org/10.3390/ijms25137477

Wang AJ, Zhang J, Xiao M, Wang S, Wang BJ, Guo Y, Tang Y, Gu J. Molecular mechanisms of doxorubicin-induced cardiotoxicity: novel roles of sirtuin 1-mediated signaling pathways. Cell Mol Life Sci. 2021;78:3105-25. https://doi.org/10.1007/s00018-020-03729-y

Wu X, Wei J, Yi Y, Gong Q, Gao J. Activation of Nrf2 signaling: A key molecular mechanism of protection against cardiovascular diseases by natural products. Front Pharmacol. 2022;13:1057918. https://doi.org/10.3389/fphar.2022.1057918

Yoo MH, Gu X, Xu XM, Kim JY, Carlson BA, Patterson AD, Cai H, Gladyshev VN, Hatfield DL. Delineating the role of glutathione peroxidase 4 in protecting cells against lipid hydroperoxide damage and in Alzheimer's disease. Antioxid Redox Signal. 2010;12:819-27. https://doi.org/10.1089/ars.2009.2891

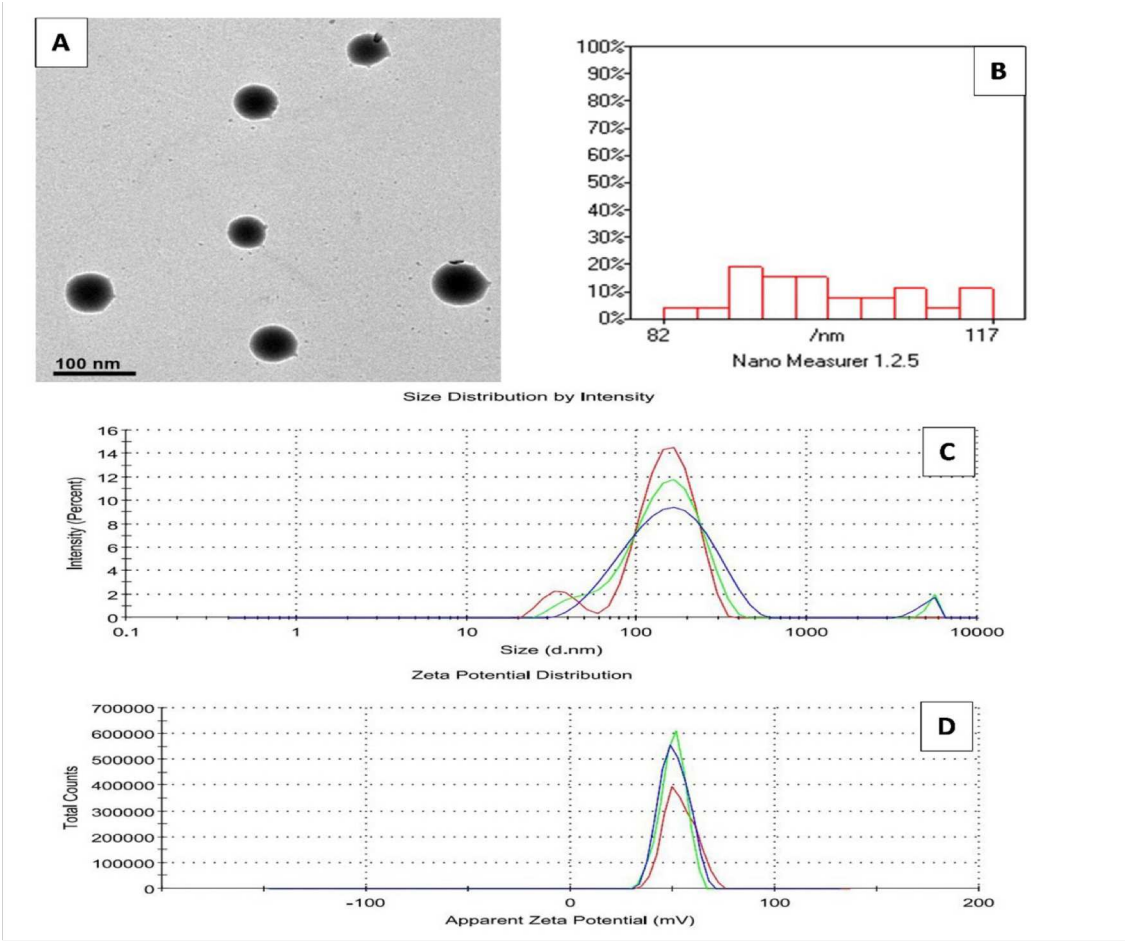

Figure 1. Physicochemical Characteristics of NOB-CSNPs. (A) Nobiletin-Loaded Chitosan Nanoparticle (NOB-CHNP) morphology by TEM. (B) Cumulative results showing particles cluster distribution between 82 nm and 117 nm. C) Z-diameter distribution by volume. D) Zeta potential distribution.

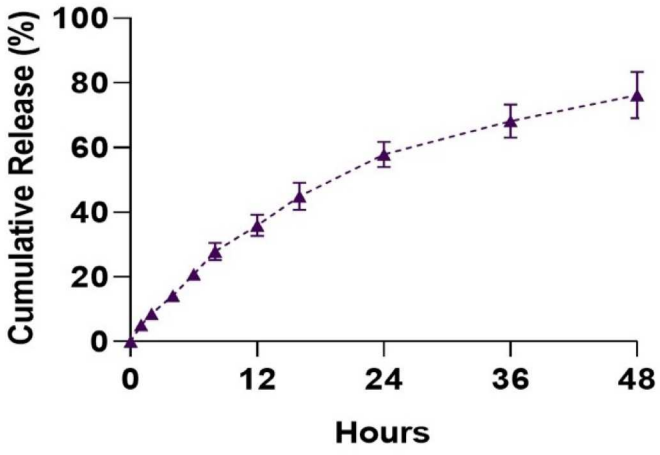

Figure 2. In vitro release of NOB. Sustained Nobiletin release from Chitosan-Based Nanoparticles over 48 h.

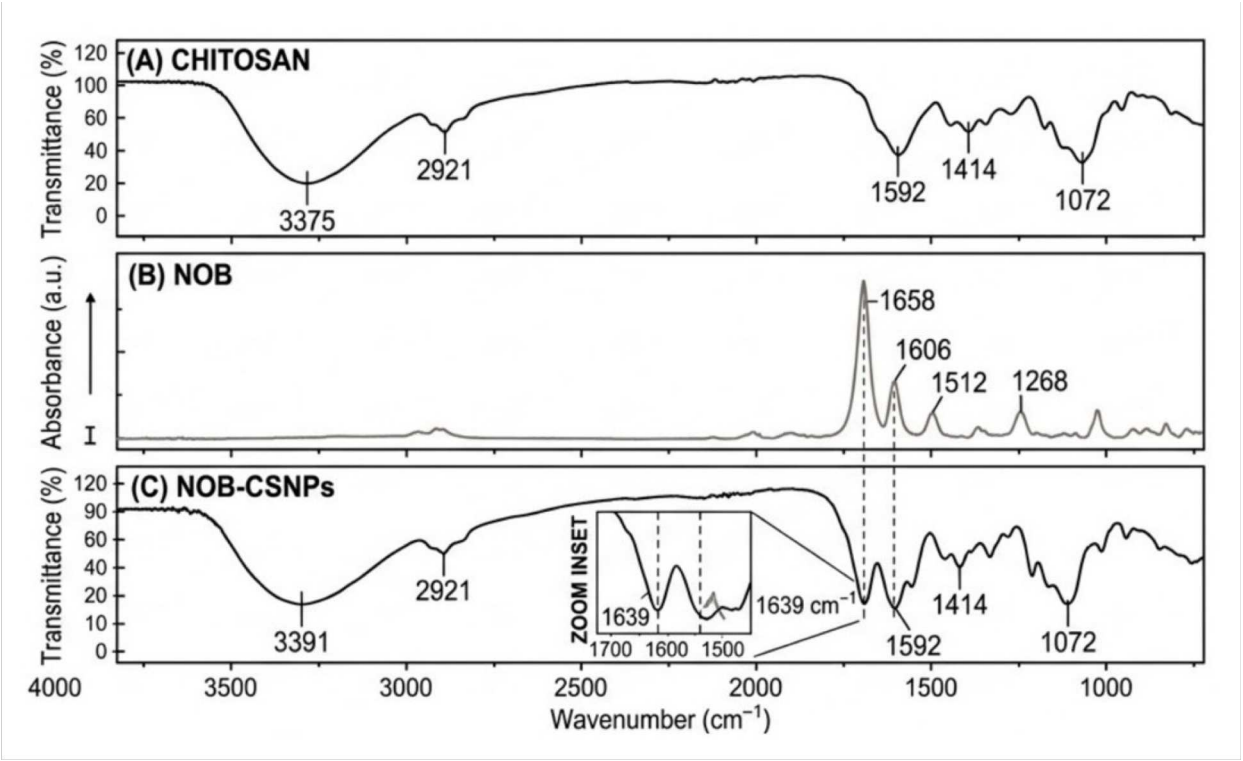

Figure 3. Comparative FTIR Spectral Analysis of Nobiletin, Chitosan, and Nobiletin-Loaded Chitosan Nanoparticles. (A) The chitosan spectrum showing the characteristic broad O–H/N–H band around 3375 cm^{-1}. (B) The characteristic NOB-associated band near 1658 cm^{-1}. (C) After NOB-CHNP nanoparticle formation, several changes in band position and intensity are seen. The broad O–H/N–H band now appears around 3391 cm^{-1} and the NOB-associated band appears at 1639 cm^{-1}.

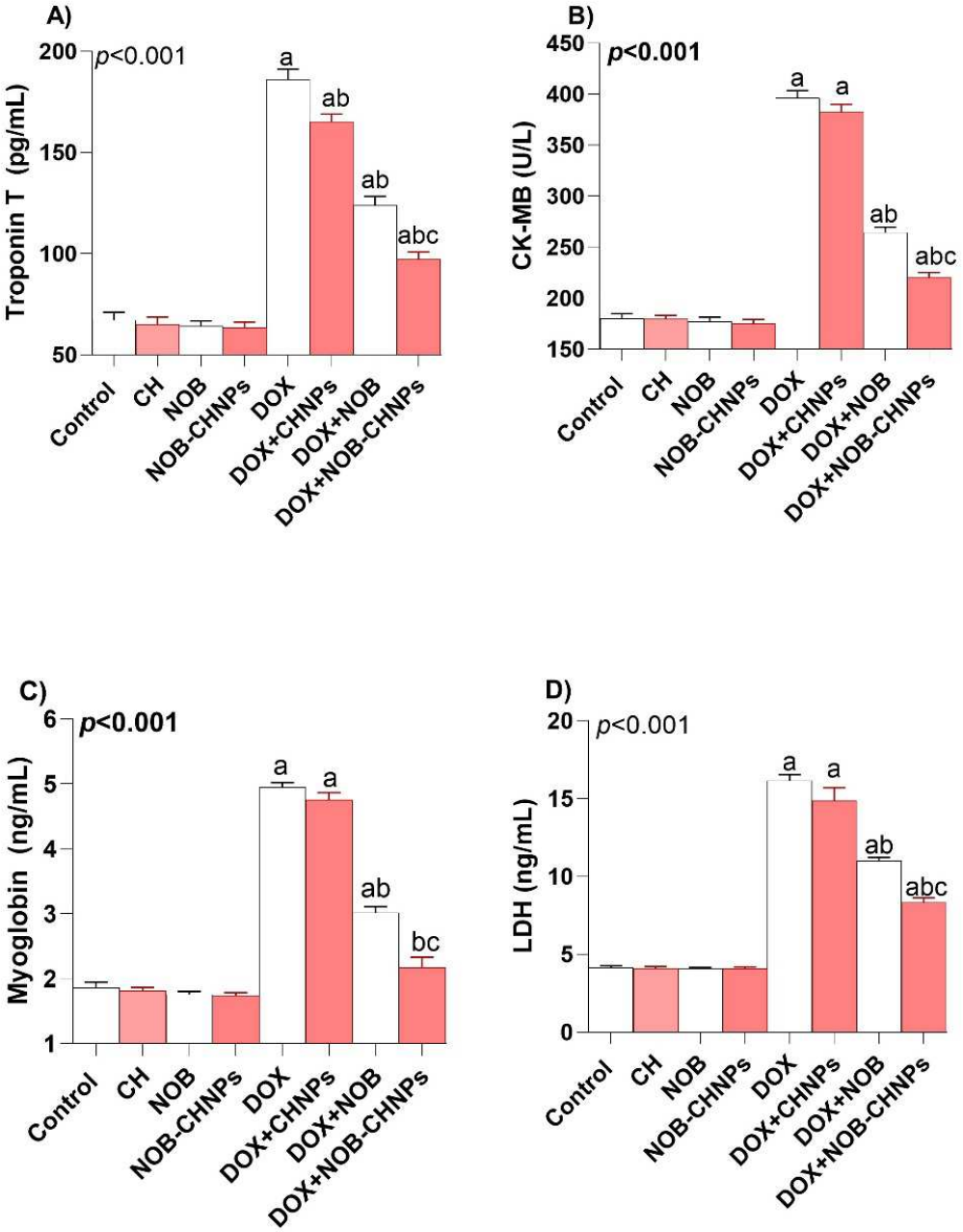

Figure 4. Effect of Nobiletin and Nobiletin-Loaded Chitosan Nanoparticles on Serum Troponin T (TnT) (A), Creatine Kinase-MB (CK-MB) (B), Myoglobin (MYO) (C), and Lactate Dehydrogenase (LDH) (D) Levels in Doxorubicin-Treated Rats. Data are shown as mean ± SEM. Statistical significance was defined as $p<0.05$. Different superscript letters (a–c) indicate significant between-group differences relative to the normal control (a), DOX-exposed (b), and crude NOB-treated (c) groups.

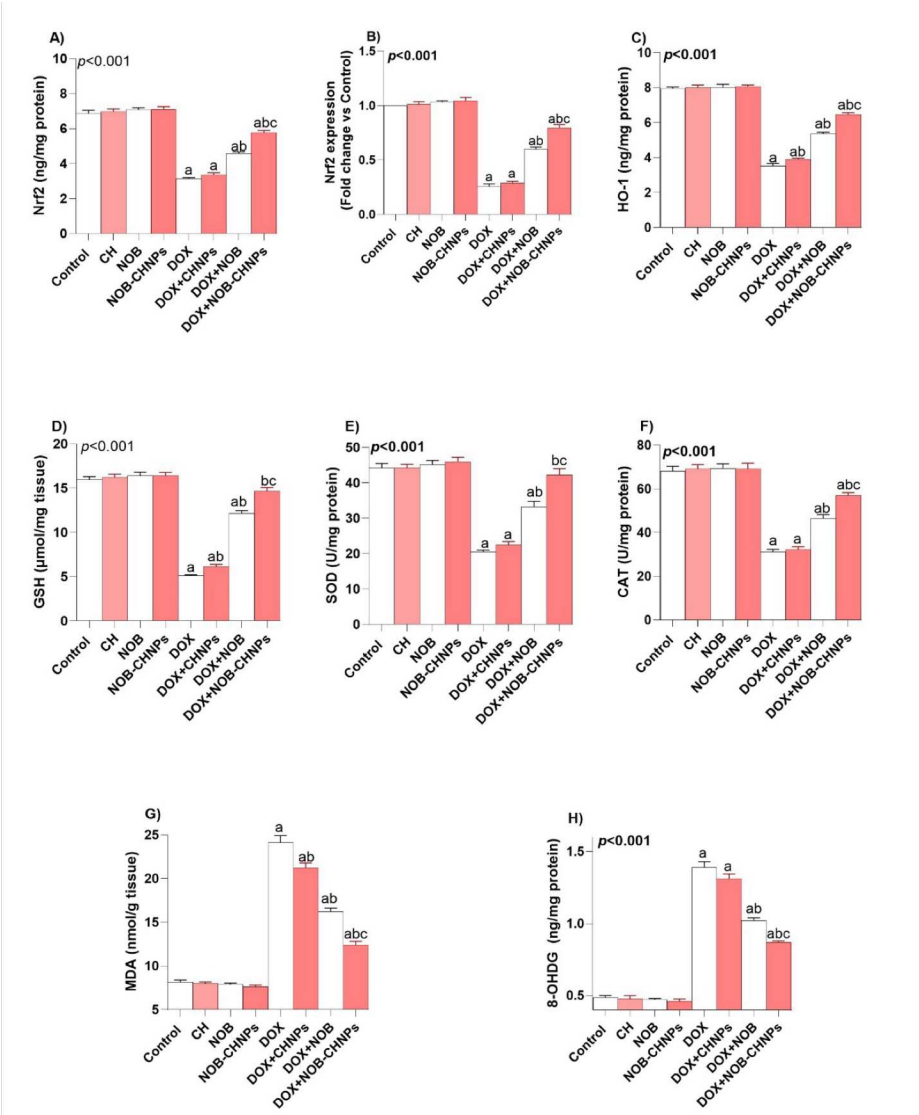

Figure 5. Effect of NOB and NOB-CHNPs on Myocardial Oxidative Stress and Antioxidant Defense. Effects of NOB and NOB-CHNPs on Nrf2 protein expression (A), Nrf2 mRNA (B), HO-1 protein expression (C), Reduced glutathione (GSH) (D), SOD activity (E), Catalase activity (F), MDA levels (G), and 8-OHdG levels (H) in myocardial tissue from DOX-treated rats. Data are shown as mean ± SEM. Statistical significance was defined as $p<0.05$. Significant between-group differences are indicated by superscript letters (a–c) vs. normal control (a), DOX-treated (b), and crude NOB-treated (c) groups.

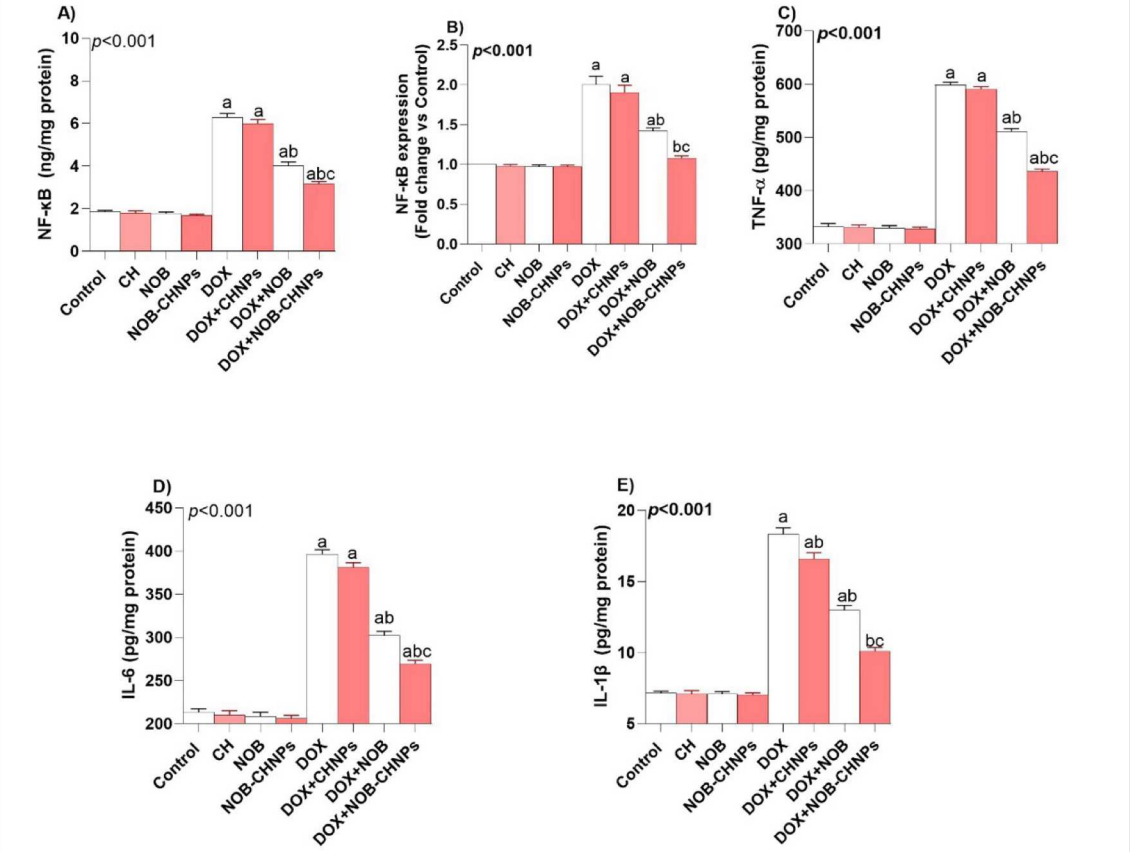

Figure 6. Effect of NOB and NOB-CHNPs on Myocardial Inflammation. Effects of NOB and NOB-CHNPs on NF-κB protein (A) and mRNA (B), TNF-α (C), IL-6 (D), and IL-1β (E) levels in myocardial tissue from DOX-treated Rats. Data are shown as mean ± SEM. Statistical significance was defined as $p < 0.05$. Statistical significance was defined as $p<0.05$. Significant between-group differences are indicated by superscript letters (a–c) vs. normal control (a), DOX-treated (b), and crude NOB-treated (c) groups.

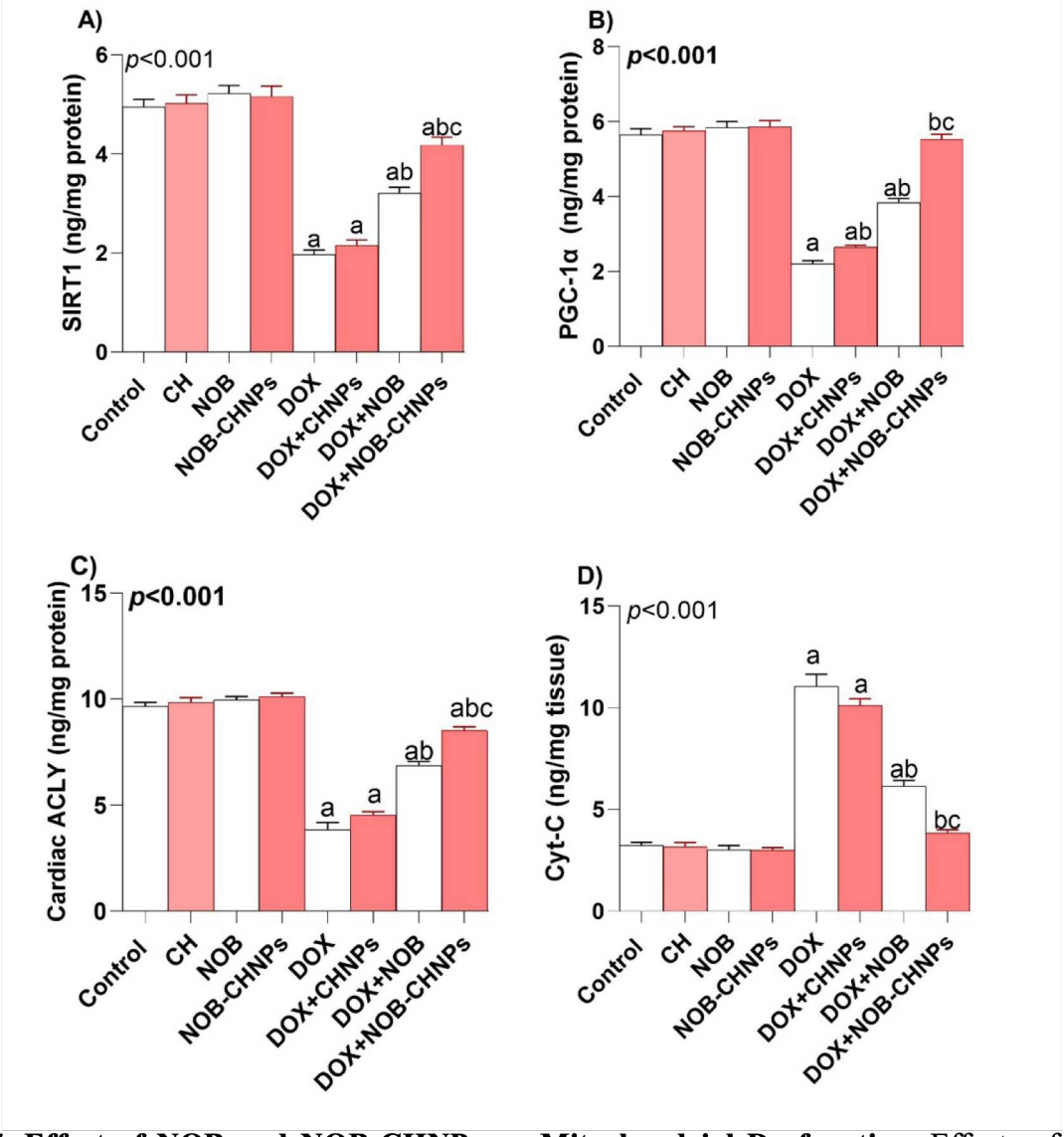

Figure 7. Effect of NOB and NOB-CHNPs on Mitochondrial Dysfunction. Effects of NOB and NOB-CHNPs on SIRT-1 (A), PGC-1α (B), ACLY (C), and Cytochrome c (D) levels in myocardial tissue from DOX-treated Rats. Data are shown as mean ± SEM. Statistical significance was defined as $p<0.05$. Significant between-group differences are indicated by superscript letters (a–c) vs. normal control (a), DOX-treated (b), and crude NOB-treated (c) groups.

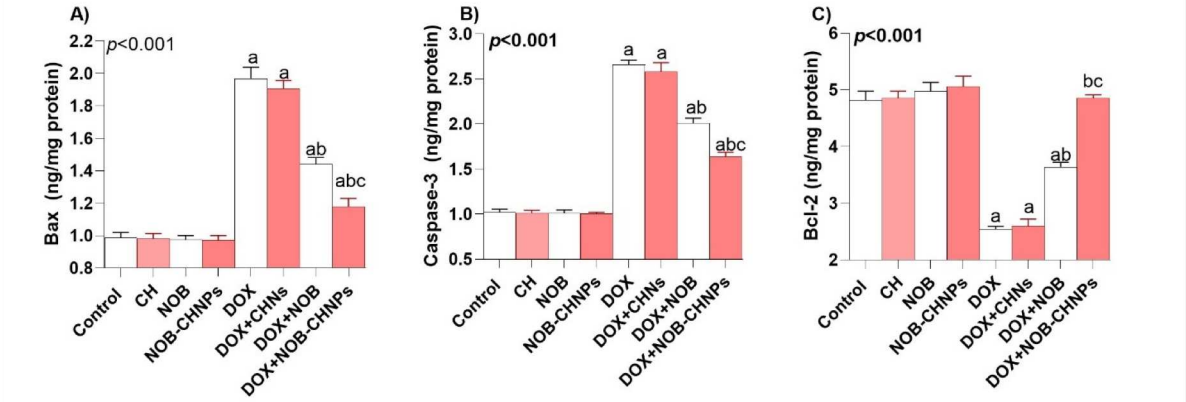

Figure 8. Effect of NOB and NOB-CHNPs on Apoptotic Markers. Effects of NOB and NOB-CHNPs on Bax (A), Caspase-3 (B), and Bcl-2 (C) levels in myocardial tissue of DOX-treated rats. Data are shown as mean ± SEM. Statistical significance was defined as $p<0.05$. Significant between-group differences are indicated by superscript letters (a–c) vs. normal control (a), DOX-treated (b), and crude NOB-treated (c) groups.

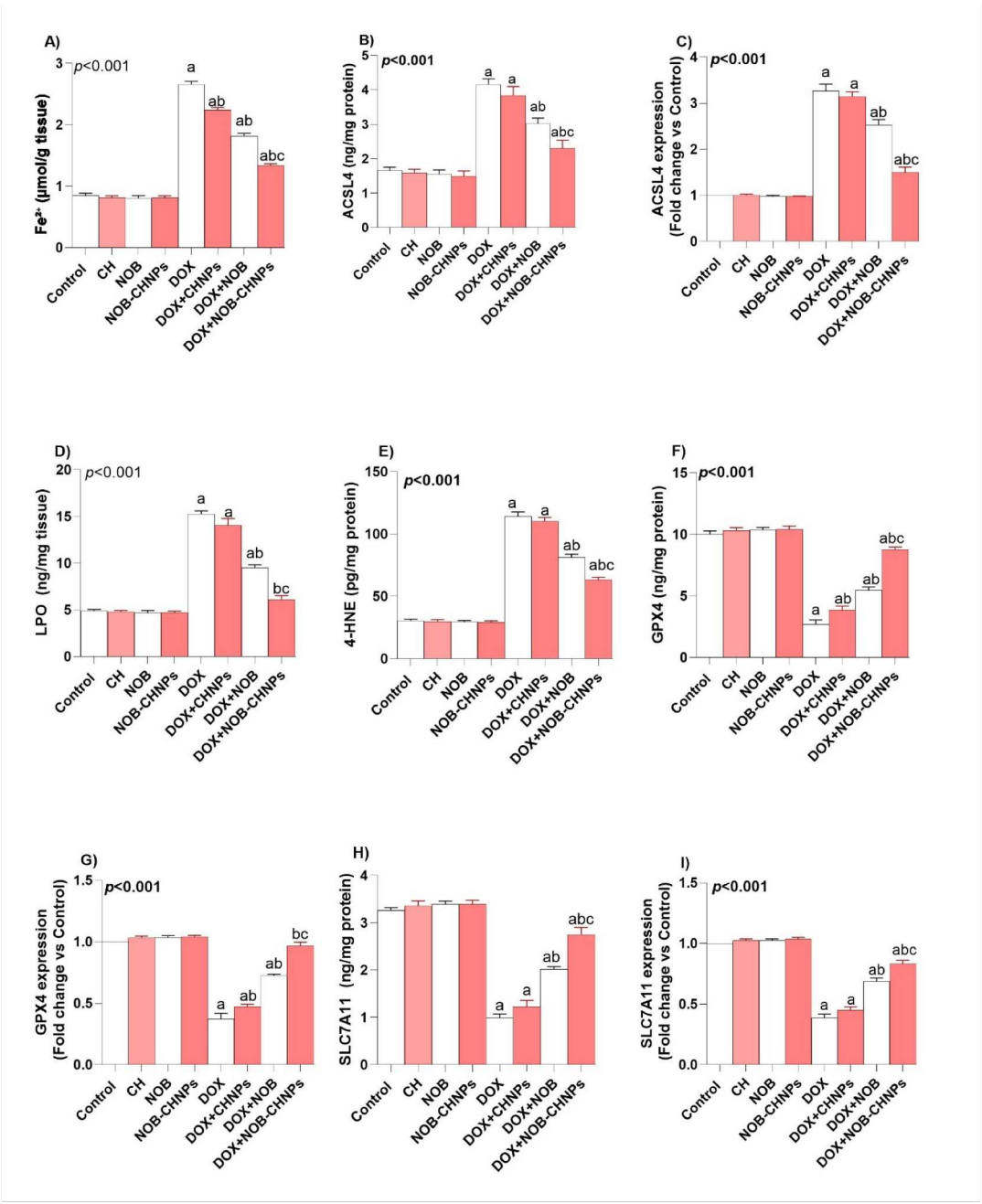

Figure 9. Effect of NOB and NOB-CHNPs on Ferroptosis Markers. Effects of NOB and NOB-CHNPs on cardiac iron content (A), ACSL4 protein (B), ACSL4 mRNA (C), Lipid Peroxidation (LPO) (D), 4-HNE **(**E**),** GPX4 protein (F), GPX4 mRNA (G), SLC7A11 protein (H), and SLC7A11 mRNA (I) levels in myocardial tissue of DOX-treated rats. Data are shown as mean ± SEM. Statistical significance was defined as $p<0.05$. Significant between-group differences are indicated by superscript letters (a–c) vs. normal control (a), DOX-treated (b), and crude NOB-treated (c) groups.

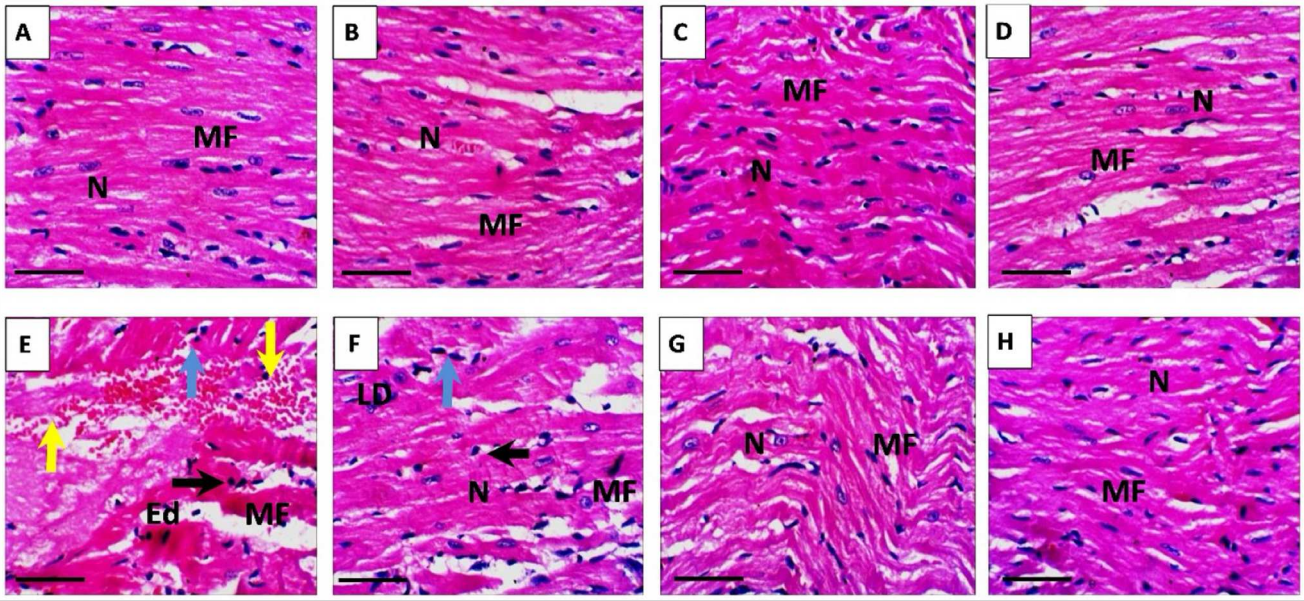

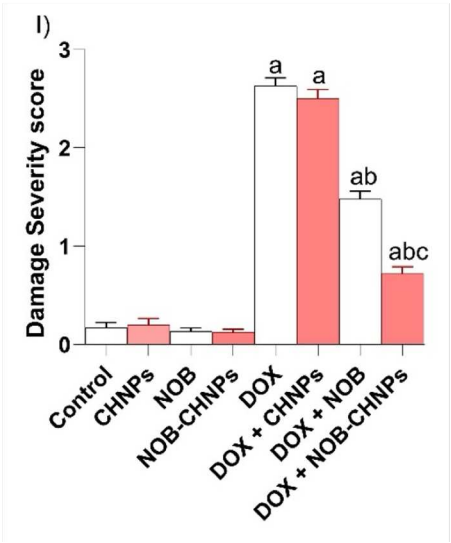

Figure 10. Effect of NOB and NOB-CHNPs on DOX-Induced Cardiac Histopathological Changes. Representative photomicrographs of H&E-stained myocardial sections from control (A), CH (B), NOB (C), NOB-CHNP (D), DOX (E), DOX+CHNP (F), DOX+NOB (G), and DOX+NOB-CHNP (H) - treated rats. N-nuclei; MF-myofibrils; Ed-interstitial edema; blue arrow- inflammatory cell infiltration; black arrow-pyknotic nuclei; yellow arrow-congested blood vessel (H&E, 400X magnification; scale bar = 50 µm).

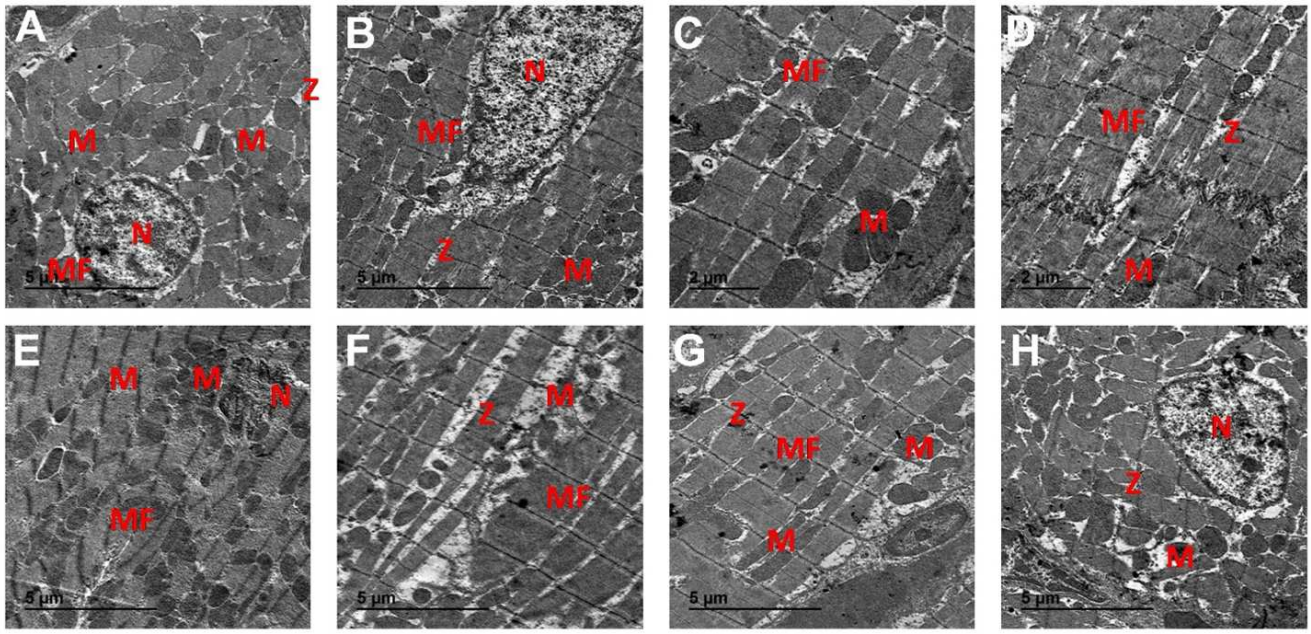

Figure 11. Effect of NOB and NOB-CHNPs on DOX-Induced Cardiac Ultrastructural Alterations. Representative transmission electron micrographs (TEM) showing cardiac ultrastructure from control (A), CH (B), NOB (C), NOB-CHNPs (D), DOX (E), DOX+CHNPs (F), DOX+NOB (G), and DOX+NOB-CHNP (H)-treated rats. MF-myofibrils; Z-Z-lines; N-euchromatic nuclei; M-intermyofibrillar mitochondria.

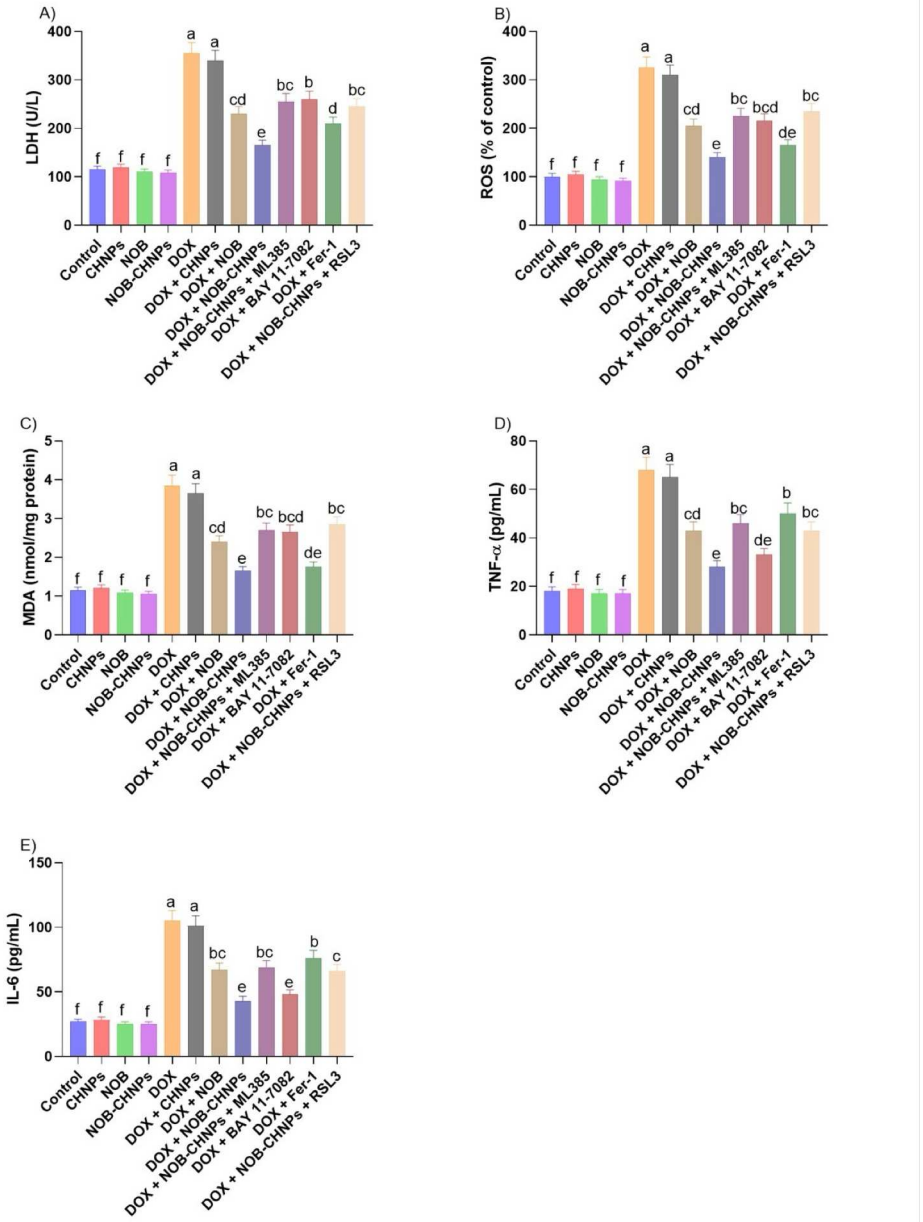

Figure 12. Effect of NOB and NOB-CHNPs on Markers of Inflammation and Oxidative Stress in Cultured Cardiac Myocytes. Primary cultures of cardiomyocytes were treated with vehicle (control), CHNP, NOB-CHNP, DOX, DOX+CHNP and DOX+NOB+CHNP, the Nrf2 inhibitor ML385, NF-κB inhibitor BAY 11-7082, ferroptosis inhibitor (Fer-1), and/or GPX4 inhibitor RSL3 as indicated. LDH release (A), intracellular ROS production (B), MDA levels (C), TNF-α levels (D), and IL-6 levels (E) were measured. Data are presented as mean ± SD of six independent biological replicates (n=6). Statistical significance was defined as $p<0.05$. Significant between-group differences are indicated by superscript letters (a–f) vs. normal control (a), DOX-treated (b), crude NOB-treated (c), DOX+NOB+CHNP-treated (d-f) groups.

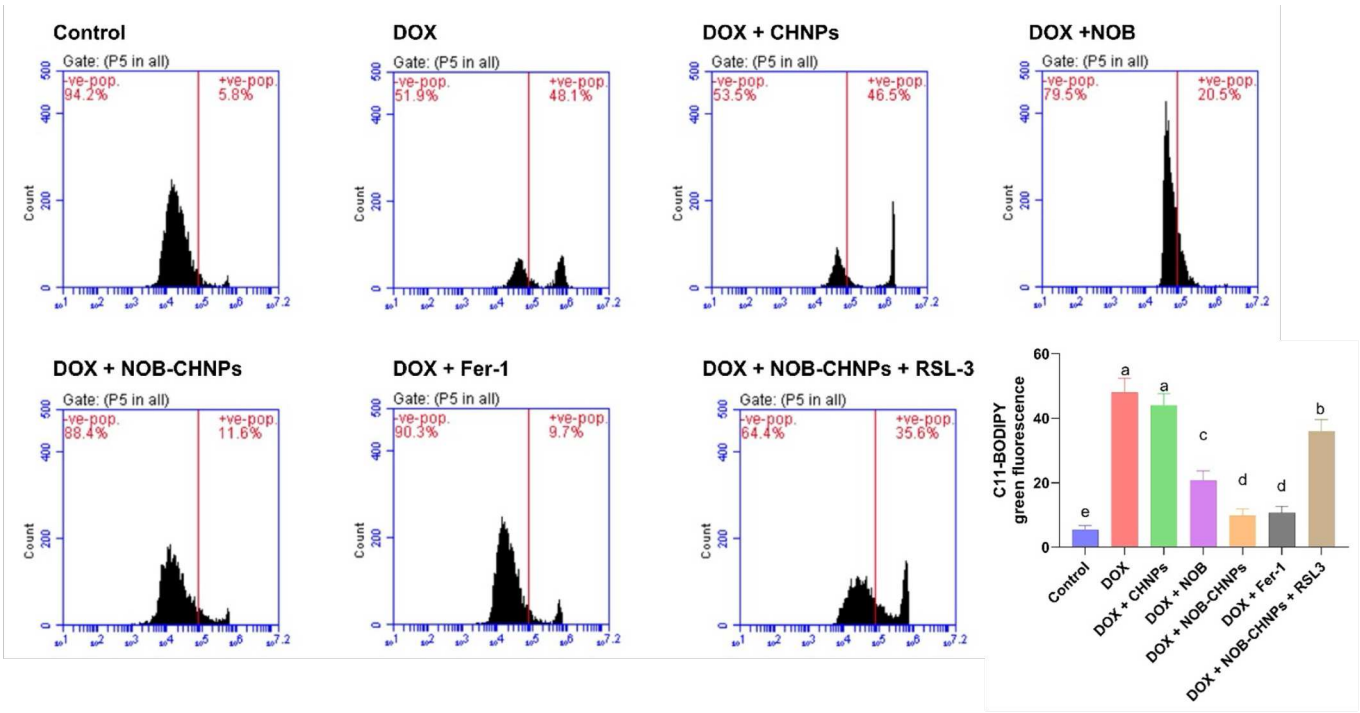

Figure 13. Effect of NOB-CHNPs and ferroptosis modulators on DOX-induced lipid peroxidation in primary cardiomyocytes. (A) Representative flow-cytometry histograms of oxidized C11-BODIPY fluorescence in the control, DOX, DOX + CHNPs, DOX + NOB, DOX + NOB-CHNPs, DOX + Fer-1, and DOX + NOB-CHNPs + RSL3 groups. (B) Quantitative analysis of C11-BODIPY oxidation (% positive cells). Data are presented as mean ± SD of six independent biological replicates (n=6). Statistical significance was defined as $p<0.05$. Significant between-group differences are indicated by superscript letters (a–d) vs. normal control (a), DOX-treated (b), crude NOB-treated (c), DOX+NOB+CHNP-treated (d) groups.